A Comodulation Analysis of Atmospheric Energy Injection into the Ground Motion at InSight, Mars

Constantinos Charalambous[1], Alexander E Stott[1], Tom Pike[2], John McClean[1], Tristram Warren[3], Aymeric Spiga[4], Donald Banfield[5], Raphaël F. Garcia[6], John Clinton[7], Simon C. Stähler[8], Sara Navarro López[9], Philippe Henri Lognonné[10], Taichi Kawamura[11], Martin van Driel[12], Maren Böse[13], Savas Ceylan[13], Amir Khan[14], Anna Catherine Horleston[15], Guénolé Orhand-Mainsant[16], Luis Mora Sotomayor[9], Naomi Murdoch[17], Domenico Giardini[12], and William Bruce Banerdt[18]

[1]Imperial College London
[2]Imperial College
[3]Oxford
[4]Sorbonne Université (Faculté des Sciences)
[5]Cornell
[6]Institut Supérieur de l'Aéronautique et de l'Espace SUPAERO
[7]Swiss Seismological Service
[8]Eidgenössische Technische Hochschule Zürich
[9]Centro de Astrobiología
[10]Institut de Physique du Globe de Paris et Université de Paris Diderot
[11]IPGP
[12]ETH Zürich
[13]ETH Zurich
[14]Swiss Federal Institute of Technology
[15]University of Bristol
[16]ISAE-SUPAERO
[17]ISAE SUPAERO
[18]Jet Propulsion Laboratory

November 23, 2022

Abstract

Seismic observations involve signals that can be easily masked by noise injection. For InSight, NASA's lander on Mars, the atmosphere is a significant noise contributor for two thirds of a Martian day, and while the noise is below that seen at even the quietest sites on Earth, the amplitude of seismic signals on Mars is also considerably lower requiring an understanding and quantification of environmental injection at unprecedented levels. Mars' ground and atmosphere provide a continuous coupled seismic system, and although atmospheric functions are of distinct origins, the superposition of these noise contributions is poorly understood, making separation a challenging task. We present a novel method for partitioning the observed signal into seismic and environmental contributions. Pressure and wind fluctuations are shown to exhibit temporal cross-frequency coupling across multiple bands, injecting noise that is neither random nor coherent. We investigate this through comodulation, quantifying the signal synchrony in seismic motion, wind and pressure. By working in the time-frequency domain, we discriminate the origins

of underlying processes and provide the site's environmental sensitivity. Our method aims to create a virtual vault at InSight, shielding the seismometers with effective post-processing in lieu of a physical vault. This allows us to describe the environmental and seismic signals over a sequence of sols, to quantify the wind and pressure injection, and estimate the seismic content of possible Marsquakes with a signal-to-noise ratio that can be quantified in terms of environmental independence. Finally, we exploit the temporal energy correlations for source attribution of our observations.

A Comodulation Analysis of Atmospheric Energy Injection into the Ground Motion at InSight, Mars

C. Charalambous[1], A. E. Stott[1], W. T. Pike[1], J. B. McClean[1], T. Warren[2], A. Spiga[3,4], D. Banfield[5], R. F. Garcia[6], J. Clinton[7], S. Stähler[8], S. Navarro[13], P. Lognonné[10,4], T. Kawamura[10], M. van Driel[8], M. Böse[7,8], S. Ceylan[8], A. Khan[8,9], A. Horleston[11], G. Orhand-Mainsant[6], L. M. Sotomayor[13], N. Murdoch[6], D. Giardini[8]and W. B. Banerdt[14]

[1]Department of Electrical and Electronic Engineering, Imperial College London, London, UK
[2]University of Oxford, Department of Physics, Parks Road, Oxford OX1 3PU, UK
[3]Laboratoire de Météorologie Dynamique, Sorbonne University, Paris, France
[4]Institut Universitaire de France, 1 rue Descartes, Paris, France
[5]Cornell Center for Astrophysics and Planetary Science, Cornell University, Ithaca, NY, USA
[6]Institut Supérieur de l'Aéronautique et de l'Espace SUPAERO, Toulouse, France
[7]Swiss Seismological Service, ETH Zurich, Zurich, Switzerland
[8]Institute of Geophysics, ETH Zurich, Zurich, Switzerland
[9]Institute of Theoretical Physics, University of Zurich, Zurich, Switzerland
[10]Université de Paris, Institut de physique du globe de Paris, CNRS, Paris, France
[11]School of Earth Sciences, University of Bristol, Bristol, UK
[12]Max Planck Institute for Solar System Research, Göttingen, Germany
[13]Centro de Astrobiologia (INTA-CSIC), 28850 Torrejón de Ardoz, Madrid, Spain
[14]Jet Propulsion Laboratory, California Institute of Technology, Pasadena, CA, USA

Key Points:

- A comodulation analysis is implemented to describe and interpret the sensitivity of InSight's seismometers to atmospheric energy injection
- The seismic response of InSight to the wind and pressure is observed to vary diurnally and seasonally depending on atmospheric conditions
- The power from the wind and pressure signals injected into seismic events is quantified to assess marsquake discrimination

Corresponding author: Constantinos Charalambous, `constantinos.charalambous@imperial.ac.uk`

Abstract

Seismic observations involve signals that can be easily masked by noise injection. For InSight, NASA's lander on Mars, the atmosphere is a significant noise contributor impeding the identification of seismic events for two thirds of a Martian day. While the noise is below that seen at even the quietest sites on Earth, the amplitude of seismic signals on Mars is also considerably lower, requiring an understanding and quantification of environmental injection at unprecedented levels. Mars' ground and atmosphere provide a continuous coupled seismic system, and although atmospheric functions are of distinct origins, the superposition of these noise contributions is poorly understood, making separation a challenging task. We present a novel method for partitioning the observed signal into seismic and environmental contributions. Atmospheric pressure and wind fluctuations are shown to exhibit temporal cross-frequency coupling across multiple bands, injecting noise that is neither random nor coherent. We investigate this through comodulation, quantifying the signal synchrony in seismic motion, wind and pressure. By working in the time-frequency domain, we discriminate the origins of underlying processes and provide the site's environmental sensitivity. Our method aims to create a virtual vault at InSight, shielding the seismometers with effective post-processing in lieu of a physical vault. This allows us to describe the environmental and seismic signals over a sequence of sols, to quantify the wind and pressure injection, and estimate the seismic content of possible Marsquakes with a signal-to-noise ratio that can be quantified in terms of environmental independence. Finally, we exploit the temporal energy correlations for source attribution of our observations.

Plain Language Summary

InSight put the first seismic station on the surface of another planet in 2019. While it has made the first detection of marsquakes, the wind has been providing a strong background signal. This work aims to separate out the unwanted injection from the atmosphere on Mars to give us confidence when we are seeing vibrations from the planet itself. To do this we use measurements from InSight's wind and pressure sensors.However, we see no stable relationship between how strongly the wind is blowing and how much vibration we pick up on our seismometers. Also, we are mainly sensing the wind shaking the lander, which in turn is transmitting its vibrations to the ground under our seismometer. These complications have led us to use the measurements themselves to work out the strength of the environmental injection rather than rely on a complex time-varying model of the possible pathways. We show how we can work out estimates of how much the atmosphere is affecting our seismic measurements and in particular show that the strongest possible quakes we have detected are above what we might have expected from just the measurements from our wind and pressure sensors at the time.

1 Introduction

The InSight seismic station on Mars is the first geophysical observatory ever deployed on the surface of another planet (W. B. Banerdt et al., 2020). It has recorded the quietest seismic traces observed since the Apollo mission, owing to the lack of anthropogenic noise and oceanic microseismic noise on Mars (Lognonné et al., 2020). However, unlike on the Moon, strong motion due to local atmospheric injections dominates the data for much of the Martian day (sol). This was previously observed by the Viking's seismic experiment (Anderson et al., 1977; Lorenz et al., 2017) where the on-deck seismometer was mostly affected by wind coupling. This impact of such a site noise level on the ability for an on-deck deployment to perform seismology was established in Panning et al. (2020).

In light of the lessons learned from the Viking mission, InSight invested much effort in the deployment of the Seismic Experiment for Interior Structure (SEIS) seismometer.

As the mission's critical scientific instrument, SEIS was developed with the prime focus on recording ground motions caused by seismic events, offering a unique and unprecedented opportunity for identifying marsquakes or meteorite impacts. The SEIS assembly design is comprised of an independent three-axis seismometer duo: the oblique very broad band (VBB) and short period (SP) seismometers (Lognonné et al., 2019). SEIS measurements are complemented with the on-deck mounted Auxiliary Payload Sensor Suite (APSS, see (Banfield et al., 2018; Spiga et al., 2018)), monitoring environmental conditions to help limit the impact of Mars' local atmosphere fluctuations on SEIS over both short and long time-scales, via continuous high-rate pressure, temperature and wind measurements (Temperature and Winds for InSight (TWINS)). A robotic arm (Trebi-Ollennu et al., 2018) was included to move the SEIS assembly from the lander deck to a precise area on the ground and then cover it with the Wind and Thermal Shield (WTS). As such, InSight has been able to operate as a seismic observatory on Mars and has detected several regional and distant marsquake events (Giardini et al., 2020).

Although this careful deployment and subsequent shielding has proved significant in reducing the noise level for InSight, and below that seen at the quietest sites on Earth over much of its observational bandwidth, the seismic traces still exhibit clear correlation with the environmental conditions and so their analysis is required. Lander-induced vibrations that predominantly originate from variations observed in the atmosphere, induce regolith displacements through elastic deformations and continuously couple to the seismic signal. This was predicted in pre-landing assessments (Lognonné & Mosser, 1993; Murdoch et al., 2017; Mimoun et al., 2017). The observed relationships are complex and exhibit non-linear coupling dynamics, complicating investigation of any seismic signals. In this work we introduce a comodulation framework to determine the complex relationships that emerge from the continuous coupled system between the atmosphere and ground acceleration, and quantify the noise contribution to the seismic signal. Our method is applied to the detected marsquakes to quantify their independence from environmental contamination and help discriminate the origins of observed seismic features. Finally, we show that the comodulation approach can be applied to retrieve wind speed and direction, and also the pressure fluctuations over short and long time-scales.

2 Background

On Earth, much research has gone into minimizing the background noise in seismic observations. While this is bounded by instrument sensitivity, the installation most often provides the limiting factor in terms of site-noise injections across the recording bandwidth (Ringler et al., 2020). A significant driver of this noise is a sensitivity to the environmental parameters of temperature, pressure and wind either through first-order forcing or second-order coupling (Johnson, Vernon, et al., 2019). Such coupling could arise, for example, from the transferred energy of wind-induced motion on local trees or structures to the shallow subsurface (Johnson, Meng, et al., 2019). These have linked and overlapping contributions and we here focus on the pressure and wind sources.

The injection into the seismic record has several modalities which each impact different frequency bandwidths. Low frequency injections with periods above 10s, are relatively well understood physically. For the vertical component, the pressure force begins to dominate (Ziolkowski, 1973; Zürn & Widmer, 1995) whereas the horizontal experiences tilt from both pressure and wind effects (G. G. Sorrells, 1971; G. Sorrells et al., 1971; G. G. Sorrells & Goforth, 1973; De Angelis & Bodin, 2012). This direct forcing is accentuated by local site characteristics including the ground material and vault/installation topology, which induce extra effects based on material response and forcing on nearby objects (Dybing et al., 2019; Johnson, Meng, et al., 2019; Wolin et al., 2015).

Site contributions extend to higher frequencies and recent studies on the wind induced noise have performed statistical analyses across arrays to determine the spatial variation

(Johnson, Meng, et al., 2019; Lott et al., 2017; Dybing et al., 2019; Hutt et al., 2017). Lack of local coherence between stations has been reported (Dybing et al., 2019) showing that turbulence causes a complicated set of features which can produce tremor-like waveforms causing confusion when searching for low SNR local events (Johnson, Meng, et al., 2019). This injection modality includes high frequencies above 1 Hz (Withers et al., 1996). A theoretical approach to high frequency injections considering shear stress on site features requires a thorough knowledge of the site's characteristics (Naderyan et al., 2016). The sensitivity across a broadband range (0.1-100Hz) has been examined in Lott et al. (2017) where it is found that wind speed and direction are important as local topology and slope winds play a part. In general, the intermediate seismic bandwidth (0.1-1Hz) is dominated by the microseism and so environmental effects are rarely observed even in moderate noise sites (Dybing et al., 2019). In contrast, for InSight this is the prime observational bandwidth, and so our analysis requires quantifying environmental injection at unprecedented levels compared to terrestrial seismology in a bandwidth which has has been comparatively little studied.

With respect to the InSight mission, a noise model was developed prior to landing. Its aim was to describe and predict the noise contributions from different sources including those excited by the wind and pressure (Mimoun et al., 2017). This model identifies that the major injections will consist of:

1. Instrument self-noise
2. Temperature/thermoelastic sensitivity
3. External magnetic fields
4. Ground tilt
5. Lander motion

The ground tilt and lander motion are the analogous modes to the low and high frequency injection pathways discussed in the Earth literature. At longer periods, this tilt is predominantly the response of the ground to direct forcing from the pressure field (Lognonné & Mosser, 1993; Kenda et al., 2017b, 2020) and so a coherency analysis can be performed leading to a decorrelation (Garcia et al., 2020). Tilt can also be caused by wind forcing on the lander and WTS. In fact, the lander injection was predicted to be a significant contributor (Murdoch et al., 2017) and as Mars lacks ocean-generated microseism, these injections will be observed across the full bandwidth. This mode is the analogue of the coupling of wind from nearby structures and plants on Earth (Johnson, Meng, et al., 2019) and causes vertical motion in additional to tilt seen in the horizontal components. This has been analysed in terms of the drag and lift forces on the lander in Murdoch et al. (2017). Teanby et al. (2017) and Myhill et al. (2018) produced an analysis of how such forcing would couple through the regolith, using analogue studies in Iceland to inform the contribution to the noise model. Furthermore, the lander has several resonances which are excited by the wind (Murdoch et al., 2018). As a result, the contributions are expected to be multiple and complex.

Understanding these atmospheric contributions is further complicated when only one seismic station is available; spurious signals cannot be rejected through local array correlations as is commonly performed on Earth. On the other hand, as there is lower background ambient seismicity on Mars, the injection mode can be examined across the full bandwidth. This means that approaches to tackle the wind and pressure injections should be separable from the seismic signal at lower amplitudes, potentially leading to better techniques for the study on Earth.

In this work we introduce a novel approach in which to analyse the sensitivity of the seismometer response to injections with an environmental source across the full-bandwidth. In doing so, we are able to determine the independence of seismic events and other observed features. This allows building of a virtual vault, where noise factors are attenuated by post-processing of the seismic output rather than physically attenuated at the input to the

seismometer. Conversely, the method can further exploit the quantified seismic and pressure sensitivity and be applied in reverse to obtain estimates for predictions of the atmospheric variables, for both the wind speed and wind direction.

3 Data

To help constrain the atmosphere-induced noise contribution into the seismic signal, InSight is measuring multiple environmental parameters continuously at a high sampling rate and accuracy: wind speed and direction, temperature, pressure and the vector magnetic field, using APSS (Banfield et al., 2018). The TWINS sensors measure winds facing in opposite directions in the east and west directions, and stand at slightly different heights of less than 10 cm due to InSight's tilt in its landed position on Homestead hollow (Banfield et al., 2020). A detailed study of the characteristics and meteorological phenomena observed from InSight's atmospheric science instrument data are described in Banfield et al. (2020).

Data are recorded continuously at 1 Hz for the wind, 20 Hz for pressure, with both variables transmitted at adjustable frequencies depending on the available data bandwidth (frequencies varying between 0.1 Hz and 1 Hz for the wind sensor and between 2 Hz to 20 Hz for the pressure sensor.) Seismic data is recorded continuously and downlinked at 20 Hz for the VBB. The SP records continuous 100 Hz, but transmits at 20 Hz. Downlink requests for specific events of interest allow small time-windows of pressure, wind and SP data to be transmitted at the higher recorded rates.

In this paper, we focus on the continuous data (InSight Mars SEIS Data Service, 2019). This allows for longer durations of uninterrupted data, permitting a deeper investigation into the atmospheric coupling measured by SEIS. We also provide examples of some of the longest duration of uninterrupted 100 Hz data, to demonstrate the broadband characteristics of atmospheric injection into the system and any variability in the seasonal evolution.

4 Analysis of the InSight observatory's sensitivity to atmospheric conditions

4.1 The Comodulation framework

We aim to explore the injection of wind and pressure into the seismic response from 0.01Hz to 50Hz as this encompasses the range in which seismic events have been observed (InSight Marsquake Service, 2020). We adopt a data-driven analysis, the comodulation framework, to determine how the signals relate before consideration of the fundamental physics driving such relationships. This particularly builds upon the approaches discussed in (Johnson, Meng, et al., 2019; Lott et al., 2017; Dybing et al., 2019) which utilize a statistical approach. Analysis of related signals through comodulation has notably been applied to understanding monaural and binaural processes of the human auditory system, where the perceptual comparison of sound by energy content reflects both the time and frequency information in the signal (J. W. Hall et al., 1984; Buus, 1985; Richards, 1987; Verhey et al., 2003). Further interactions by comodulation were noted in electrical field oscillations in the brain during cortical cooperativity and spatial memory tasks (Bruns & Eckhorn, 2004; Shirvalkar et al., 2010). In this case, we are examining the power comodulation between signals from three different sensors that raises its own particular challenges.

To introduce this method we first consider a qualitative investigation of continuous VBB data for sols 237–239, shown in Fig. 1. In this figure, we present spectrograms for the three seismic axes, vertical (Z), north (N/S) and east (E/W), pressure and wind speed for sols 237–239 (at a solar longitude of $L_s = 59°$). The weather during this period was typical of northern spring conditions at the InSight landing site in Elysium Planitia (Banfield et al., 2020). The ambient (large-scale) wind direction is from the south-east in the daytime with

excursions from the south-west direction in the nighttime (see InSight weather observations in (Banfield et al., 2020) and pre-landing predictions in (Spiga et al., 2018)). Multiple dust devil-like convective vortices occur through the daytime, identified by an abrupt drop in the atmospheric pressure with broadband injection and ground tilt seen on SEIS. The maximum pressure drop during this 3-sol period occurred on sol 239 with a magnitude of 4.7 Pa and can be observed in Fig. 1a as a broadband impulse in the pressure and seismic spectrograms at 11.41 Local Mean Solar Time (LMST).

There is a three-regime meteorological diurnal cycle typically encountered at the InSight landing site at various seasons (Banfield et al., 2020): intense convective turbulence in the daytime between 08:00-17:00 LMST; a quiet period after sunset of low wind speed below the wind sensor's detection threshold, when Mars is quiet enough to reveal the instrument self-noise (Lognonné et al., 2020) and the majority of the identified seismic events are detected (Giardini et al., 2020); and, following a transition in wind direction (17:00-19:00 LMST), a nighttime regime with gravity waves and small-amplitude shear-driven turbulence (19:00-07:00 LMST). Although transition times between these three regimes vary on a seasonal timescale, opportunistic windows for seismic detection emerge during the low noise periods. One example of such a window is indicated by the vertical grey dashed lines in Fig. 1. The quiet periods can also be distinguished by the emergence of a continuously excited 2.4 Hz vibration, predominantly on the vertical component with an origin that is yet unknown (Lognonné et al., 2020). A 15-minute high frequency event exciting this 2.4 Hz resonance is observed at the final quiet window, at approximately 18:52 LMST in the evening prior to sol 240.
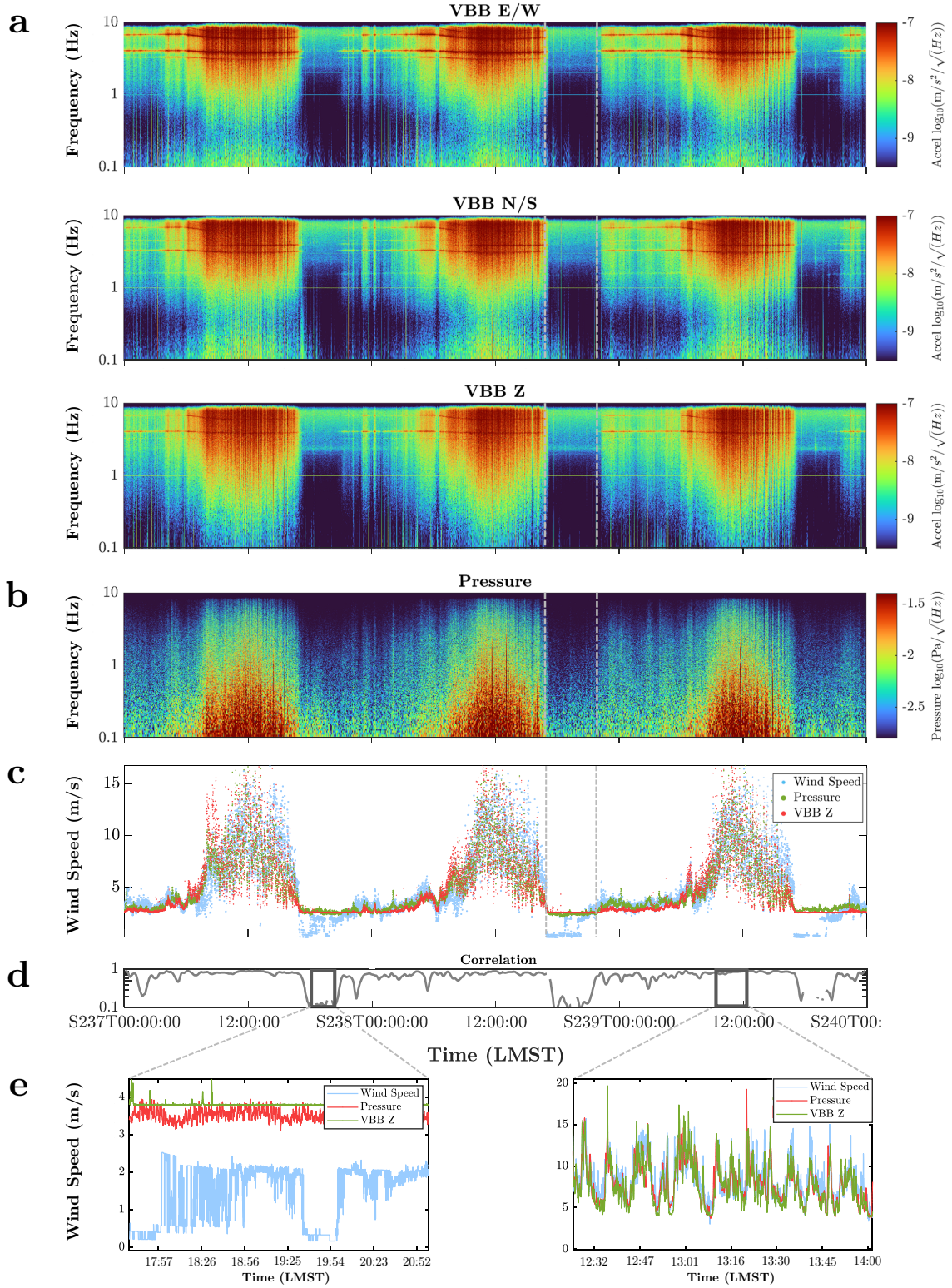
Figure 1: (a) Spectrograms of the continuous 20 Hz VBB during the sol-period 237 to 239 for all three ENZ components, respectively, (b) Spectrogram of the continuous pressure channel over the same duration (c) Wind speed data in cyan. Pressure (0.1-4 Hz) and vertical acceleration (0.1-8Hz) envelopes are here scaled by a single gain and an offset, shown in green and red, respectively. (d) Envelope correlation coefficient between the seismic acceleration response in (d) and wind speed derived in Section 4.2.1 (e - left) Magnification of the quiet period during which envelope correlation breaks down and (e - right) a period during strong correlation, showing how the daytime turbulent fluctuations dance in synchrony.

The wind speed magnitude and the power fluctuations observed in the spectrograms of pressure and ground acceleration in Fig. 1 are strikingly similar across a wide range of frequencies. Despite this, the coherence between the raw time series is often low (Garcia et al., 2020). This indicates a breakdown in the phase relationship between the signal amplitudes. To this end, we propose that the similarity of these spectrograms and the wind speed magnitude is caused by comodulation between the atmospheric and seismic signals.

The observed co-variation between the signals will be driven by the known effects previously outlined, e.g. the effect of wind on local features, tilting and vibrations. We can consider these effects by constructing a model where the measured atmospheric conditions, pressure and wind, are considered as inputs with the seismic ground acceleration as the output, that is, the response to forcing from various physical injection pathways. These include:

1. Direct forcing on the ground from the atmosphere
2. Vibrations of the lander coupled through the regolith
3. Forcing on the WTS coupled to the SEIS assembly through local ground deformations and direct forcing acting on the umbilical tether connecting the deployed instrumentation to the lander body

The response of each of these pathways is complex and the proposed comodulation framework is invoked to capture the multiple pathways and describe the full effects of the system. Hence we consider these pathways in terms of energy transfer rather than signal amplitude. This energy injection is predominantly driven by dynamic pressure P as outlined in (Murdoch et al., 2017),

$$P = \frac{\rho U^2}{2}$$

where ρ is the air density and U is the wind speed, injecting energy through various paths that include the lander, WTS and ground itself through drag forcing

$$F = SCP$$

where S is the surface area and C the drag coefficient. This highlights the many sensitivities of the system including the wind speed, the height of the object on which the force is imparted, the wind direction (which will affect the surface area with respect to the lander geometry) and the air composition. In addition, the drag coefficient of these elements is dependent on the Reynolds number, which in turn is affected by the wind properties itself. The Reynolds number characterizes the flow, which can be described by an 'orderly' laminar flow or by a 'chaotic' turbulent flow; or as transient between the two. Furthermore, the surface topography will also affect the wind properties. Although wind speed is the major variable, the relationship with pressure shown in Fig. 1 indicates this cannot be ignored in these bandwidths, whether its cause is instrumental sensitivity to wind, a joint dependence through turbulence or the introduction of additional forcing pathways.

This approach of relying on the signals themselves to quantify the injection is in contrast to the more theoretical studies in this issue (Garcia et al., 2020; Kenda et al., 2020; Murdoch et al., 2020) which found good application within certain frequency bands or during convective vortices enabling the extraction of near surface elastic properties from the physical pathway. In order to further distinguish environmentally generated seismic noise across the full bandwidth, however, future studies must handle the comodulated effects elucidated here.

4.2 Envelope calculation and comparison

The seismic acceleration and pressure spectrogram intensities are correlated along with the wind speed, and suggest power co-fluctuations, as shown in Fig. 1. To quantify this

observed comodulation relationship we examine the root mean square (RMS) envelopes, $e[t]$, which yield an estimate of the signal power. To this end we are able to capture the observed variation in the power domain. In this section we derive how these envelopes are obtained and then compared.

For a given time series $x[n]$ ($n = 1, 2 \ldots, N$) the spectrogram is calculated as a set of power spectral density (PSD) slices $X[k, t]$ for a window length W_{len} and overlap OL_{win}, where k denotes the frequency bin and t the time step at which the window is taken. The envelope is then calculated as

$$e[t] = \sqrt{\sum_{k=P}^{P+Q} X[k, t] \frac{1}{W_{len}}} \qquad (1)$$

where P and Q designate the frequency bins that equate to the desired bandwidth of study $f_{min} - f_{max}$.

4.2.1 Envelope regression through moment matching

The envelopes $e_Z[t]$, $e_N[t]$, $e_E[t]$, $e_P[t]$ and $e_W[t]$ are the signals by which we can assess the correlation between the wind, pressure and seismic measurements. The pressure and wind are termed as inputs to the system and the seismic acceleration response is the output. To this end, we would like to predict one envelope from another through a regression. We have chosen to implement the method of moments as a statistical basis for this regression (DeGroot & Schervish, 2012) a tool that has enjoyed a wide variety of applications as a common approach used for estimation in econometrics (Hansen, 1982; A. R. Hall, 2005), to determining the evolution of aerosol dynamics (McGraw, 1997).

The method of moments dictates that two time series can be matched in terms of their statistical moments, in this case with the first moment being the mean and the second central moment being the variance about the mean, In this approach, we assume one distribution to be the reference distribution, with the other being the empirical. The moments are therefore the primary parameters in determining a forecasting equation that transforms the empirical distribution, from its sample moments, to the corresponding population moments of the reference distribution (Pearson, 1894; Hansen, 1982). The method of moment approach can therefore exploit relationships by solving between unknown parameters and the moments of two distributions. This fundamentally sets up a theoretical moment equation that yields from the transformation of the time-series, in our case, to their envelopes. The moments for each variable provide solutions to the ensuing set of equations, by matching the sample moments to the reference.

For example, consider N samples of the time series $e_X[t]$ and $e_Y[t]$ stored in the vectors $\mathbf{e}_X = [e_X[1], e_X[2], \ldots, e_X[N]]$ and $\mathbf{e}_Y = [e_Y[1], e_Y[2], \ldots, e_Y[N]]$. To moment-match the time series $e_Y[t]$ to $e_X[t]$ up to second-order statistics, the mean of $\mathbf{e}_Y$ is first set to zero and the variance is normalised to one. The variance is then scaled to that of $\mathbf{e}_X$ and the mean added. Only one theoretical moment equation is required for each unknown parameter describing the time-series. This is solved by the ensuing set of equations in terms of the moments arising from the time-series of interest. An estimator is then obtained by substituting the moments evaluated from the sample to the theoretical moments of the reference time-series. This process is summarised as

$$\mathbf{e}_Y^{MM} = (\mathbf{e}_Y - \mathrm{Mean}(\mathbf{e}_Y)) \Big(\frac{\mathrm{Var}(\mathbf{e}_X)}{\mathrm{Var}(\mathbf{e}_Y)} \Big)^{\frac{1}{2}} + \mathrm{Mean}(\mathbf{e}_X) \qquad (2)$$

where the mean operator is

$$\mathrm{Mean}(\mathbf{e}) = \frac{1}{N} \sum_{n=1}^{N} e[n] \qquad (3)$$

and the variance operator is

$$\text{Var}(\mathbf{e}) = \frac{1}{N-1} \sum_{n=1}^{N} |e[n] - \text{Mean}(\mathbf{e})|^2 \qquad (4)$$

for the vector $\mathbf{e} = [e[1], e[2], \dots, e[N]]$. This is essentially a process to choose a gain and an offset to regress two time series.

This envelope is computed for the three seismic axes Vertical, $e_Z[t]$, North, $e_N[t]$, and East, $e_E[t]$ and the pressure $e_P[t]$. As noted above, the wind speed, $e_W[t]$, is already in the necessary domain for comparison. The visual similarity of Fig. 1a, b & c can therefore be quantified by comparing the wind speed to the power, as calculated using a moving RMS envelope, of the pressure and ground acceleration in different frequency bands. The wind speed, pressure (0.1–4 Hz) and ground acceleration (0.1–8 Hz) envelopes, are shown in Fig. 1c. The pressure and vertical ground acceleration envelopes are scaled and offset (using the matched moments technique) to obtain a regression to the wind speed allowing an estimate for the equivalent wind speed from the total power in each of these signals on the basis of wind-induced coupling. The correlation between signals in power as opposed to the usual amplitude is shown in Fig. 1d, where the averaged correlation between the wind speed and seismic envelope is maintained throughout the sol. The correlation indicates synchronous amplitude envelope fluctuations and therefore attributes the atmosphere as the primary noise injector masking the seismic signal.

4.3 Application of comodulation analysis for InSight

In this section we describe the generally observed relationships in terms of the comodulation at the daily and seasonal scales. The signals comodulate across the Martian sol in distinct regimes and comodulation offers a way of quantifying the distinct relationships seen during each regime. We achieve this by application of the moment-matching approach, allowing us to compare the degree of coupling between the atmospheric and seismic signals. These regimes are then analysed over a range of bandwidths to explain the full observation. We consider how these relationships have changed over the course of the mission. As the environmental components of pressure and wind are the driving factor, their relationship is then discussed. Finally we show how the wind data can be predicted from the seismic and pressure signals using the moment-matching approach.

4.3.1 Diurnal variation

We examine, first at diurnal timescales:

1. the ground acceleration response to the atmospheric variation over the course of a sol,
2. the frequency dependence of this variation,
3. the difference between vertical and horizontal acceleration response for both 1 & 2.

In order to explain the observations, we will first describe their relationships over the diurnal cycle.

4.3.1.1 Time dependence of diurnal ground acceleration:

Fig. 2c shows the vertical seismic acceleration envelope (in the 0.1-8 Hz band) against the wind speed for sols 237–239. Fig. 2a plots the pressure and temperature variations of this 3-sol period, with the vertical lines indicating the sunrise and sunset in each sol. The wind

speed is shown in (b). Over the course of these sols it can be seen that the relationship is governed by three regimes according to the wind-induced ground response. These dominant regimes in the observed acceleration coincide with the typical three-regime diurnal cycle of Mar's atmosphere at the Insight landing site, as encountered at various seasons (Banfield et al., 2020).

During the Martian sunset, a quiet period emerges when the wind drops below a threshold of $2.4\,\mathrm{m\,s^{-1}}$, with the acceleration response confined within the (**red**) tail in the distribution of Fig. 2c. We quantify this threshold as the point below which there is no correlation with the seismic signal, as we further discuss in Section 4.3.3. During this period, the acceleration response reaches the noise floor of the VBB sensor for the bandwidth under investigation. No relationship can then be established between the wind speed and acceleration envelope. Impulse excursions are seen in the seismic acceleration envelope at stationary wind speeds, attributed to short duration non-atmospheric incursions, most often due to glitches (Scholz, J.-R. et al., 2020). The variance in this period is at its lowest for the ground acceleration, in line with this being the calmest daily interval. However, due to the unreliability of wind retrieval below this threshold, the variance in the wind measurements is high.

Following the quiet period, in (**blue**), the wind speed gradually rises from $3\,\mathrm{m\,s^{-1}}$ to $6\,\mathrm{m\,s^{-1}}$ during the nighttime until dawn. The presumed mechanism taking place during this period is an atmospheric phenomenon known as nocturnal low-level jet (Banfield et al., 2020), during which the ground acceleration appears to vary much more strongly to such low amplitude wind-speed variations. This is quantified by a steep power-law relationship with an exponent of $a = 4$ (Fig. 2d). Generally, the nighttime regime is highly stable on Mars with a strong near-surface inversion, allowing only for shear-driven weak turbulence to develop, which could result into moderate jet-yielding conditions associated with weakly turbulent, close-laminar flow (Banfield et al., 2020). This weak turbulence generates a well-behaved low variance around the mean of the wind speed time-series distribution. In contrast, the variance for acceleration is high, due to increased sensitivity in this regime. This period is characterized by long-period fluctuations in the pressure, related to gravity waves and bores, while the temperature profile is stable as the surface is cooler (Fig. 2a, (Banfield et al., 2020)).
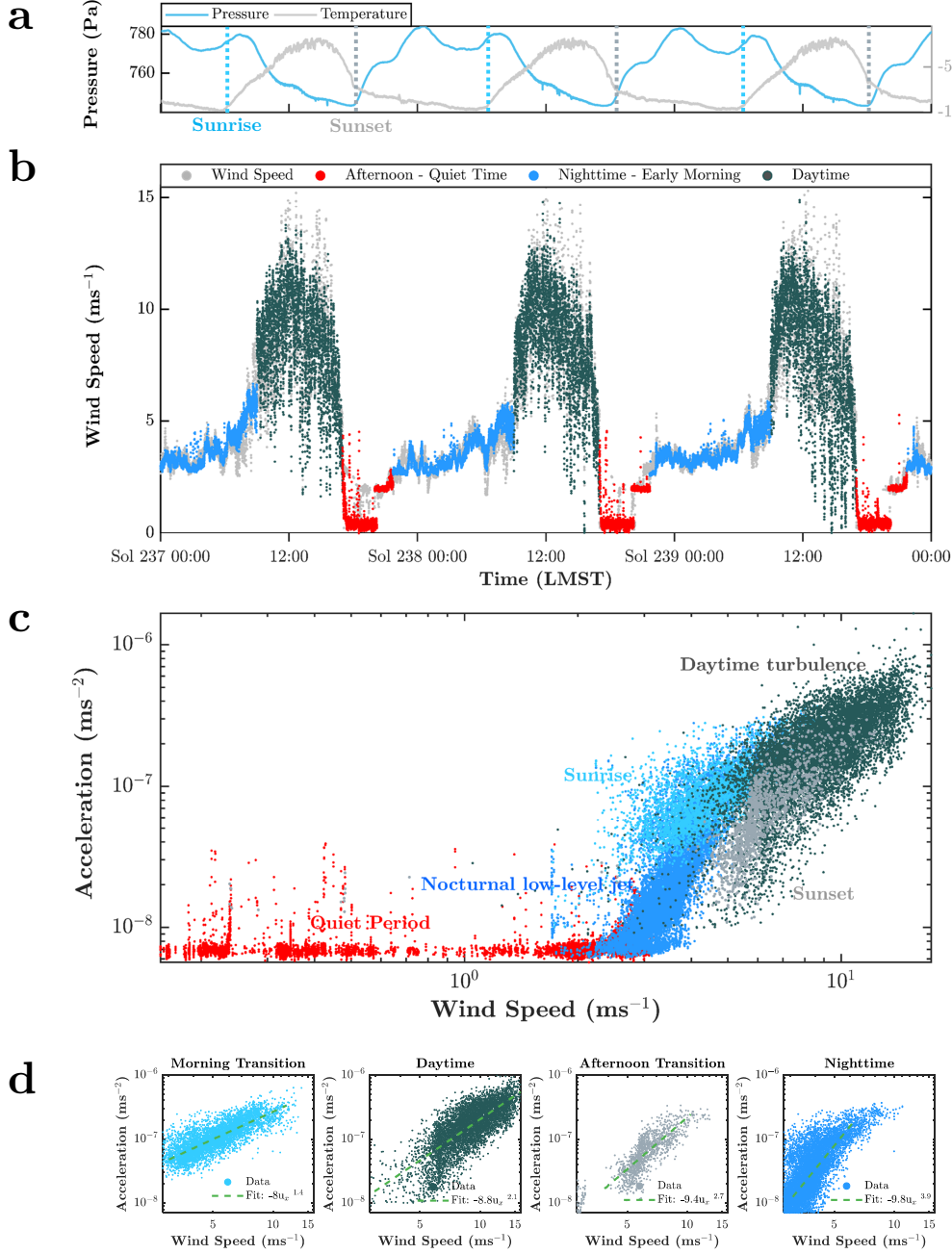
Figure 2: (a) Pressure and temperature with sunset/sunrise times annotated for sols 237-239. LMST axis time-aligned with (b) (b & c) Three main periods are evident during sols 237 - 239 investigated here, with the acceleration envelope (0.1-8 Hz) moment-matched to the reference wind speed time-series separately for each regime. In the quiet period during late afternoon, the wind drops below a threshold during which the noise approximates the noise floor of the VBB sensor (**red**). During this period no relationship can be established between the wind speed and acceleration envelope. Following this period, in (**blue**), the wind speed consistently rises slowly from $3\,\mathrm{m\,s^{-1}}$ to $6\,\mathrm{m\,s^{-1}}$ during the nighttime to the sunrise, with the ground acceleration responding much more strongly to low amplitude wind-speed variations. This regime is maintained through a steep power-law relationship with an exponent of a=4. The intensive convective turbulence regime during daytime (**dark gray**) with a power-law exponent of a=2. The transition to this turbulent regime occurs at $\sim 6\,\mathrm{m\,s^{-1}}$. In (b) we have color-coded the transitions to the regime at dawn and sunset. (c) Power-law fits (intercepts at $\log_{1}0$) to the main periods and their transitions, investigated as independent regimes.

The intense convective turbulence regime during daytime (**dark gray**) follows a shallower power law with an exponent of a = 2 (Fig. 2d). The transition to this turbulent regime occurs at a mean ambient wind $\sim 6\,\mathrm{m\,s^{-1}}$. It is characterized by the strongest wind speed fluctuations in the Martian sol, which in turn generates the highest moment values in the distribution, for both mean and variance. The short-term variance in this period is also highest for both temperature and pressure, due to rapid fluctuations

By separating these established power-law regimes, and hence providing well defined moments in the reference distribution for each segment, the moment matching technique from Eq. (2) can be applied in a piece-wise approach to provide a reasonable regression of the empirical distribution. In this case, we have transformed the acceleration domain to that of our reference, the wind speed, as shown in Fig. 2c, thus providing a measure for the equivalent wind speed, which can be seen to follow quite closely the measured one. The moment matching method captures the power-law variation through matching the logarithmic distribution in each regime using a single scaling and offset for the second-order moments.

In reality, these power-laws do not abruptly shift but follow the transitions between each regime. The rapid rise of temperature during the Martian morning imposes steep positive gradients for both the atmospheric and surface temperature (Fig. 2a), while fast cooling in the early Martian afternoon imposes an inverse temperature gradient, with such temperature swings also measured by previous missions (Hess et al., 1977; Sutton et al., 1978; Schofield et al., 1997; Davy et al., 2010; Banfield et al., 2020; Mueller et al., 2020). The transition from the nighttime to intense turbulence daytime regime takes place after sunrise, a period during which these steep atmospheric temperature gradients induce a separate short-duration regime. Similarly, the reverse occurs before sunset and as such, these effects could play a dominant role in the transitional behaviour. A detailed breakdown of these regimes and their transitions with fitted power-laws is illustrated in Fig. 2c. This indicates the presence of a short-lived linear transition during sunrise with a steeper transition during sunset.

4.3.1.2 *Frequency dependence of the ground acceleration response*

This analysis can be expanded to consider several bandwidths and include pressure, as shown in Fig. 3. The envelopes for the vertical acceleration response and pressure are computed in 0.01-0.1 Hz, 0.1-0.5 Hz, 0.5-1 Hz and 1-4 Hz bandwidths and plotted against each other and the wind speed. The pressure envelope also correlates with the seismic acceleration envelope, with similar, although less obvious regimes with relationships less dispersed compared to the wind. At the lowest frequencies, 0.01-0.1 Hz, the correlation between the seismic acceleration envelope and pressure envelope/wind speed is much weaker, and restricted to higher signal powers. This may be caused by injections not captured by the environmental sensors, such as instrument glitches. This additional non-correlated injection can be clearly seen recurring in the VBB Z row of Fig. 3a below 0.1 Hz, with a weak energy injection during the quiet period and a stronger injection occurring from midnight and extending beyond sunrise. As the frequency increases, the instrumental noise raises the seismic-signal threshold and a steeper power law represents a greater sensitivity of the seismic signal to environmental injection. In contrast, pressure and wind maintain a more consistent linear relationship, with an exponent of $a = 1$ above 0.1 Hz. Below a threshold of $2.4\,\mathrm{m\,s^{-1}}$ the response of both the pressure and seismic signals is very weak. As discussed in Section 4.1 the driving factor for the environmental injection is through the dynamic pressure. While we have shown the pressure envelope also correlates, it is the wind speed that allows the direct determination of dynamic pressure and so we will limit our analysis of the seismic injection to the wind speed before returning to this aspect in Section 4.3.3 where we will discuss the comodulation factors between all three signals.
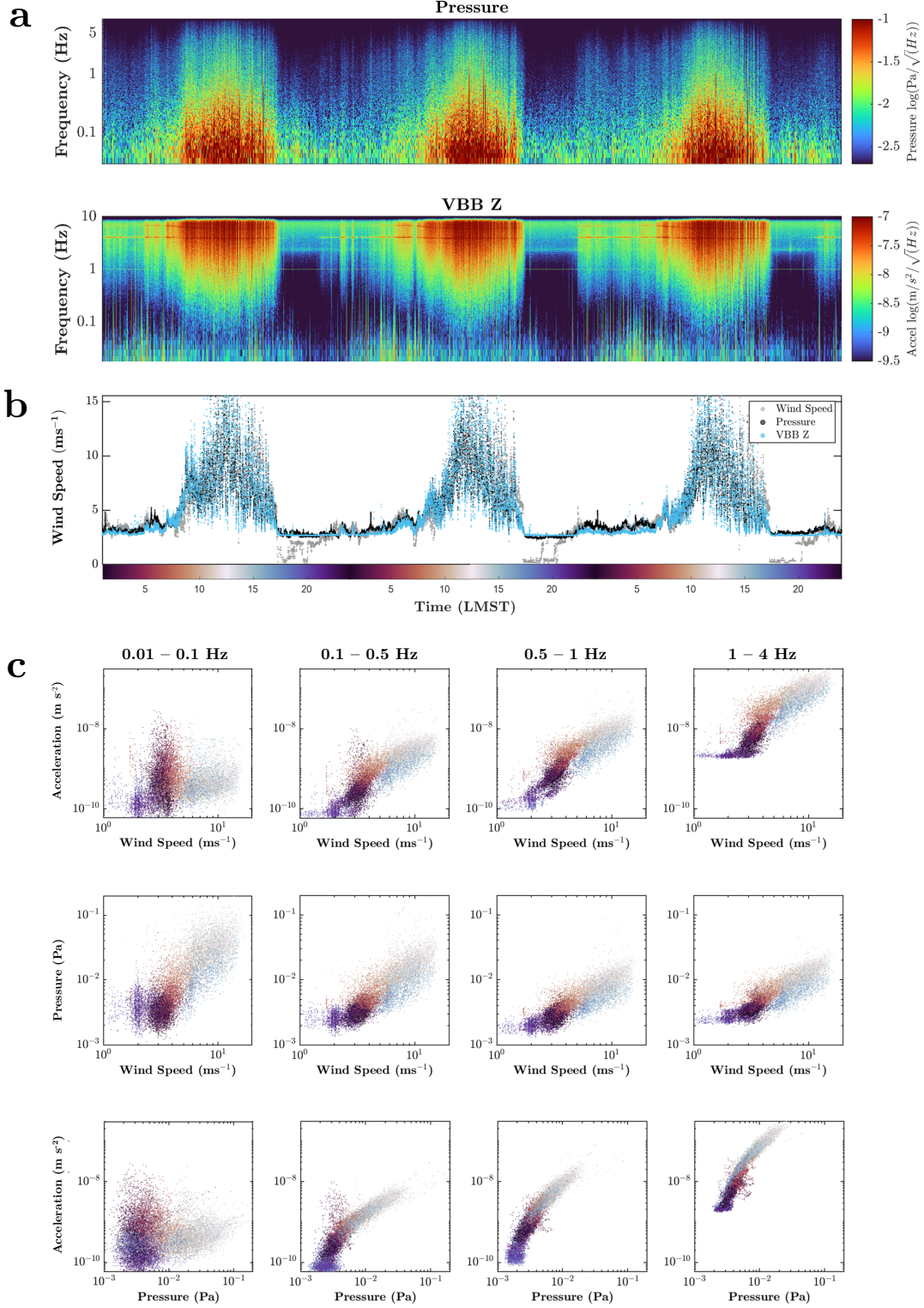
Figure 3: (a) Spectrograms for the continuous 10 Hz pressure and 20 Hz VBB Z data for sols 237–239 (b) The vertical acceleration envelope for 0.1-8 Hz and pressure envelope for 0.1-4 Hz is matched to the wind speed by a single gain and an offset over the 3 sols, based on the first two moments of the wind speed. This is time-synced to (a), with the time axis color-coded in LMST. (c) Relationships between the pressure and vertical acceleration envelopes, and wind speed, plotted over increasing frequency bands computed in 0.01-0.1 Hz, 0.1-0.5 Hz, 0.5-1 Hz and 1-4 Hz bandwidths. For both pressure and ground acceleration a wind speed threshold of about $2.4\,\mathrm{m\,s^{-1}}$ is observed, consistent with (Lognonné et al., 2020). A linearity between the wind speed and pressure is evident, indicating that pressure is a good predictor of the wind speed above the threshold.

Considering the full bandwidth from the detected marsquake event range to the antialiasing filter cut-off (0.1-40 Hz) observed by SEIS, similar correlation relationships are followed, as shown in Fig. 4 for both VBB and SP data for sols 361–362. In pane c, the acceleration response envelopes (frequencies of 0.1-1 Hz, 1-8 Hz and 8-40 Hz) are this time indicated for all three components; the East, North and Vertical, plotted against the wind speed. These sols take place in the early-summer (solar longitude of $L_s = 115°$), in contrast to the mid-spring depicted in Fig. 2. Here, the typical three-regime cycle of the weather is repeated, however, the ground acceleration indicates changes in its response. This is further addressed under the seasonal variation in Section 4.3.2. Each weather regime is well described by a power-law relationship over increasing bandwidths, similar to as observed above in Fig. 3. There is a pronounced increase in each slope with increasing frequency, indicating a higher sensitivity under the same weather fluctuations. Nevertheless, all bandwidths still share a wind-speed threshold, bounding the acceleration envelope to the ambient noise limit of that frequency range. The threshold here for these two sols 361–362 has increased to $\sim 2.8\,\mathrm{m\,s^{-1}}$, slightly above the threshold observed for sol 237–239 at $\sim 2.4\,\mathrm{m\,s^{-1}}$.

To track how frequency-related relationships change with wind speed, pane d of Fig. 4 shows the average power spectrum of the three-component seismic signal as a function of the wind speed from 0.1-10 Hz on the VBB and from 10-40 Hz on the SP. The dominant feature in this representation is the concentration of energy in mechanical modes evident as horizontal features at their resonant frequencies. These prominent modes are associated with the lander body, solar panels, instrument deployment arm, load shunt assembly and tether, co-exciting with surges in atmospheric activity. Such features are also observed on Earth, for example, resonant modes in ocean-bottom seismometer attributed to head-buoy cables strumming from fluid motion, even at moderate current velocities (Stähler et al., 2018). Here, a further characteristic of the wind speed threshold is apparent, the abrupt attenuation of modes below < 10 Hz at the $2.8\,\mathrm{m\,s^{-1}}$ wind-speed threshold. The high frequency bandwidth (8-40 Hz) exhibits increased scatter in the acceleration compared to the lower frequencies in all three regimes of the weather's diurnal pattern, as illustrated by Fig. 4b. This is owed to the persistence of multiple superimposed resonant modes and features below the wind speed threshold at higher frequencies, suggesting an excitation mechanism other than wind or pressure. The variance below the threshold is even further amplified by the frequent occurrence of a distinct class of spikes, called 'Donks', impulse-like high-frequency (>8 Hz) occurrences likely from elastothermal relaxation exciting the mechanical resonances as seen in Fig. 4d (Lognonné et al., 2020). These very short-duration excursions cannot be attributed by the energy observed in either atmospheric variable.

4.3.1.3   *Comparison of vertical and horizontal ground acceleration response*

The horizontal east and north components follow similar power laws to the vertical for all the frequency bandwidths examined in Fig. 4c. The transition between the regimes occurs at the same wind speed for all three components, with the threshold at $\sim 2.8\,\mathrm{m\,s^{-1}}$ distinguishing the quiet period for sols 361–362. A further corner point at $4\,\mathrm{m\,s^{-1}}$ seen in Fig. 4d represents the nighttime regime in our exemplar sols up until sunrise. During this period the 2.4 Hz resonance is excited below a boundary set at $4\,\mathrm{m\,s^{-1}}$ particularly on the vertical component. This excitation disappears for higher wind speeds along with the 1 Hz tick noise - electrical crosstalk between the seismic channels and the temperature house-keeping channels - observed on the N/S and Z. Above 10 Hz it can be seen that there are persistent modes even below the wind thresholds, with their intensity increasing with wind speed for all three components. For example, there is a particularly strong resonance at 25 Hz.

However, at the lowest frequencies < 0.3 Hz the seismic power increases with wind speed only on the horizontal components, likely through a tilt injection as described in (Murdoch et al., 2017). Even during the more turbulent parts of the day, the higher and lower frequency injections on the horizontal seismic components maintain a relatively undisturbed frequency

gap, only beginning to merge at ∼0.3 Hz during the stronger wind speeds. Owing to the injection by separate mechanistic processes, this frequency noise isolation suggests a possible bandwidth for event detection in the horizontal components even during more turbulent periods, something not applicable to the vertical. No events have been recorded to-date within this frequency band during the daytime.
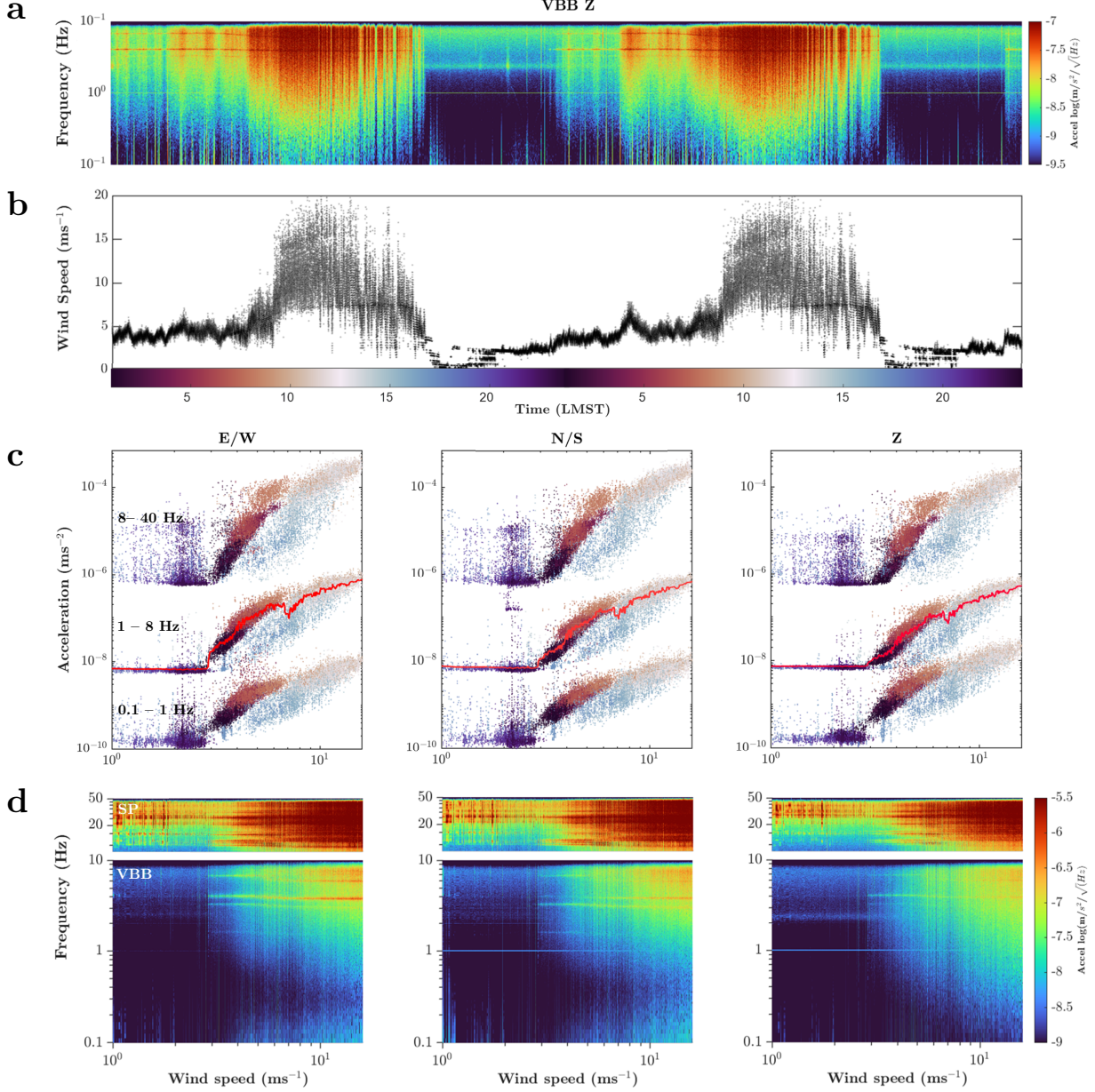
Figure 4: Spectrogram of the VBB Z acceleration for sols 361-362 is shown at the top pane. The wind speed follows, with the time axis color-coded in LMST. Note the similarity in the total seismic intensity to the wind magnitude. The third pane demonstrates the relationships that arise over the three main frequency bands, 0.1-1 Hz (VBB-bottom), 1-8 Hz (VBB-middle) and 8-40 Hz (SP-top). The bottom row shows the histogram of the atmospheric injection of wind speed per frequency bin in the acceleration signal over the same period. Overlaid in red is the mean acceleration calculated at each wind speed bin from the bottom row.

4.3.2 Seasonal changes

The diurnal comodulation relationships have been driven by the cycle of convective daytime and shear-driven nighttime turbulence and the Martian seasons trigger a change in these cycles. Fig. 5 compares the wind speed and envelope correlations for the (previously examined) bandwidths 0.1-1 Hz, 1-8 Hz and 8-40 Hz calculated on data from sols 98–99, 290–291 and 361–362 corresponding to a Martian late winter, late spring and early summer, respectively (seasons are indicated for the northern hemisphere). The selection of these sols is based upon availability of 100 samples per second (sps) seismic data. It can be immediately observed that the correlation relationships between wind speed and acceleration response envelopes do not follow a single trajectory, but rather exhibit seasonality with shifting patterns in the expected three-regime diurnal cycle of the weather.

These three cases offer a good sample of the different environmental conditions met by InSight in the first 400 sols of operation (Figure 7 in Spiga et al. (2020)). On the late-winter sols 98–99, close to spring equinox, InSight experiences high surface temperatures and particularly low ambient wind speed. Conversely, on the late-spring sols 290–291, close to summer solstice, surface temperatures reach a seasonal low while ambient wind speed is strong. The early summer period for sols 361-362 features a surface temperature on the rise again with ambient wind speed remaining strong. Of all those three cases, sols 98–99 are characterized by the strongest wind gustiness (Figure 9 in Spiga et al. (2020)).

The sols 98–99 are turbulent throughout, the mean ambient wind speed is low, and the relationship is maintained predominantly within a single regime described by a single power-law. Because the surface temperature is at its highest during these two sols (Mueller et al., 2020) and wind speed is low (Spiga et al., 2020), this could lead to purely buoyancy-driven convection throughout the sol. While sols 98–99 fall mainly within a single regime there is considerable variance. Furthermore, the noise floor is not reached due to the absence of a calm period. The high variance across this period is seen by different sensitivities to the ground acceleration for the same wind speeds and neighbouring local times of occurrence. This increased sensitivity is observed particularly in the nighttime up to dawn.
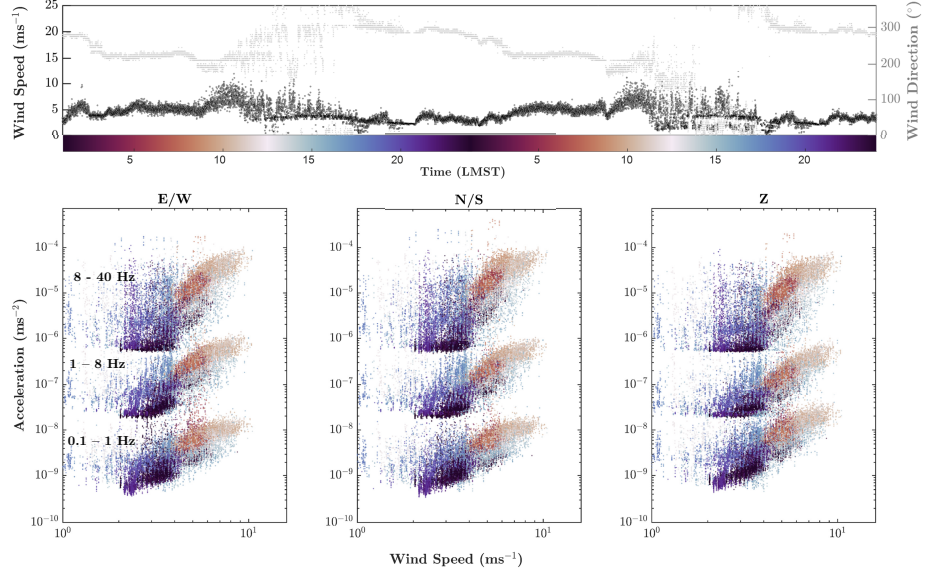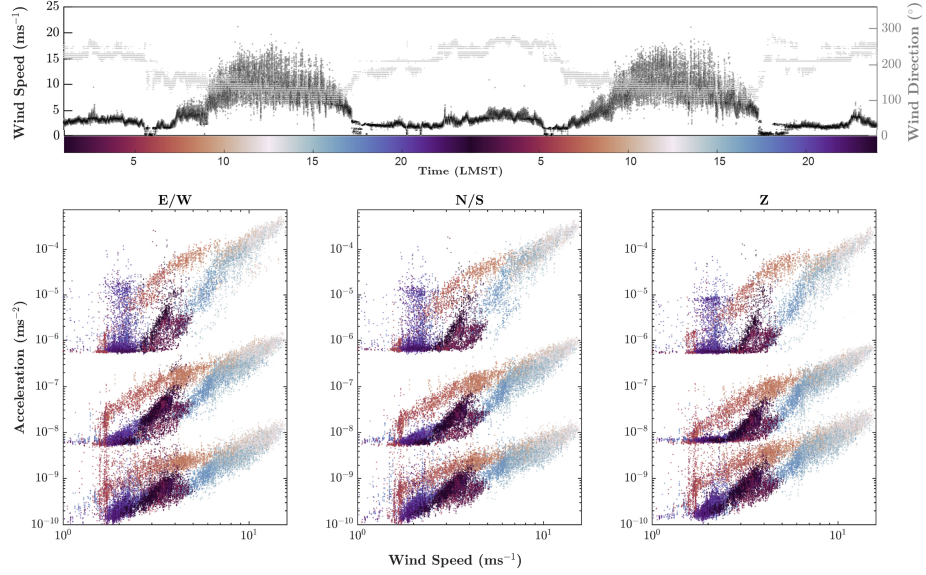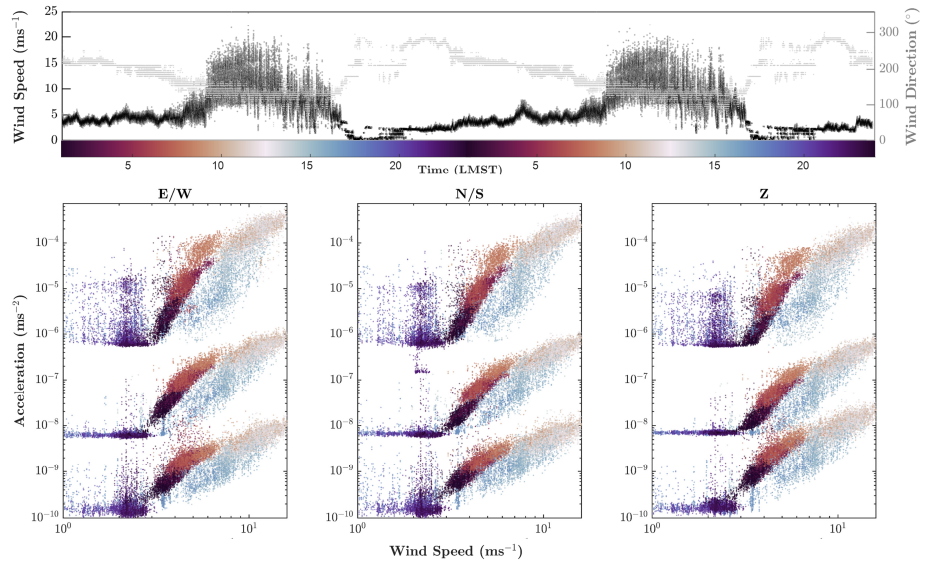
Figure 5: Seasonal dependency of the wind-seismic relationship that could arise from different external parameters such as temperature, pressure and air density.

For sols 290 and 291, the acceleration response trajectory during nighttime is split into at least three paths. During the distinct inertial oscillations caused by the low-level jet weak turbulence two of the pathways are observed; the first emerges around midnight and a further one at 4 am. The latter transitions to a flat region before re-emerging shortly after sunrise from ~ 6 to 9 am LMST, characterized by increased seismic injection compared to other sols appearing as an outlier with a clear trajectory, Although it is well matched to the steeper power law as observed in other sols, this divergence reveals a prominent feature. Upon closer inspection, this behaviour matches a reversal to the wind direction during the weakly turbulent, close laminar flow of the low level jet stream. This regime matches to a power-law exponent of 2 for 0.1–1 Hz, and further continues into the daytime turbulence. The quiet period is enteered at a lowest wind speed threshold close to $\mathrm{m\,s^{-1}}$. compared to the other two. The flat slope of the quiet period is more strongly evident at the two higher bandwidths, with the donks apparent in a cluster at 8 to 40 Hz, before the re-emergence of comodulation after midnight for a period, returning to the flat region for a short period before the injection rises again. For the 0.1-1 Hz band the whole sequence is almost along a single power law aside from a branch of higher sensitivity during the morning.

On sols 361-362 the three regimes are present similarly to sols 237–239 with clearly defined trajectories. The nighttime regime here can be seen gradually climbing up along a steep power-law trajectory, with the local time distinctly identified. After sunrise, the morning turbulence injects the highest energy but follows a shallower power law of approximate a=2 for the 0.1-1 Hz, with this slowly shifting in its intercept until sunset. At the transition to the quiet period this enters back to a steeper power law with lower injection after noon, likely due to density shift, giving the greatest separation of the daytime branches. It then promptly enters the regime with the wind speed below the threshold, identified here at $2.8\,\mathrm{m\,s^{-1}}$. The lack of injection during the quiet period is distinct at all frequencies with the highest wind-speed threshold of the three periods.

For the latter sols 290–291 and 361–362, there is an increase in both ambient wind speed and turbulence which is seen injected into the ground acceleration. The regimes are more clearly separated with more variable power-law relationships. The daytime regime preserves the relationship to a power-law close to 2. The power-law begins at the strongest ground deformations early in the day, while slowly shifting down to lower responses under similar wind magnitudes in the afternoon. This negative shift in acceleration could be related to the shift in the air density through the day, triggered by steep temperature gradients at the onset of the sun rising, and the transition of the sun setting. A denser air in the nighttime to early morning would exert a higher dynamic pressure on the surrounding elements inducing a stronger lander-coupled motion for the same wind speeds experienced through the day. This can be seen as the high variability in the acceleration envelope during the nighttime under relatively low wind speeds, forming a steep power law relationship. In contrast, a less dense air from the daytime heating will weaken up the wind-induced lander motion. Since the evolution through each regime essentially maintains a single power-law with a shift in the intercept, this could provide an alternative way of determining the Martian air density variation at InSight.

In summary, these changes in the diurnal variation previously discussed 4.3.1 are driven by the changing wind profile across the seasons, shown in Fig. 5. For sols 98–99 the wind speed is generally low with indistinct regimes and a constant low-level turbulence as measured by its high wind gustiness (Spiga et al., 2020). For late spring into early summer, the turbulent daytime increases in length and strength. As a result, it can be concluded that the seismic signal's sensitivity to the environment depends on specific weather conditions such as atmospheric pressure, wind direction, turbulence intensity/gustiness, air and ground temperature. It should be added that these conditions also affect the TWINS sensor calibration. TWINS is calibrated to retrieve the Reynolds number at the sensor position, and shows a lower measuring threshold for Reynolds numbers of approximately 100. This translates to a seasonal variable wind speed threshold value at sunset given the pressure

⁵⁷² and temperature evolution. The measured wind speed threshold would range at sunset
⁵⁷³ from $2\,\mathrm{m\,s^{-1}}$ to $2.8\,\mathrm{m\,s^{-1}}$ for sols included in this study. Complete seasonal coverage by
⁵⁷⁴ InSight over two martian years will help confirm the trends observed in this study.

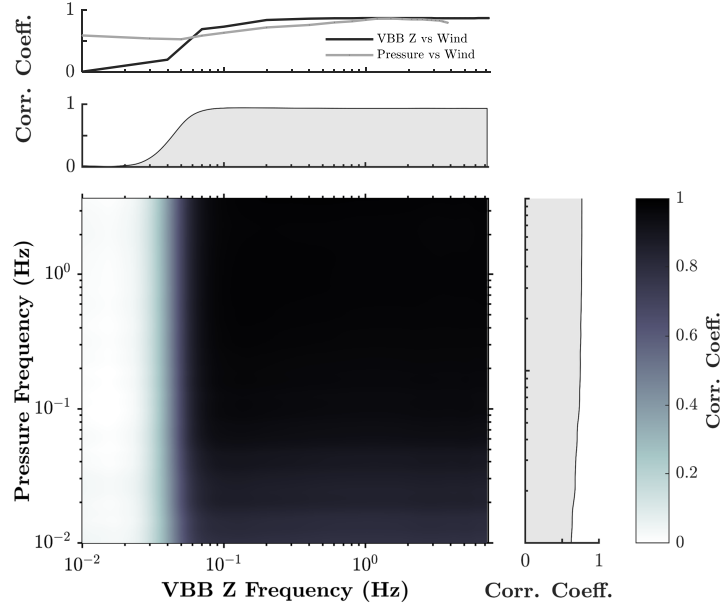⁵⁷⁵ *4.3.3 The relationship between pressure and wind*

Figure 6: This figure establishes the cross-frequency interactions between the atmosphere and ground acceleration. Co-fluctuations in amplitude-amplitude power of seismic and pressure with the wind magnitude oscillations are a prominent feature that persists diurnally. (Top) Envelope correlation coefficient for sols 237-239 between pressure and wind, and vertical acceleration and wind. The distance between each pair of points represents the frequency band at which the pressure or VBB Z signals were band-passed and envelopes extracted. The calculation for the correlation coefficient was subsequently applied to this extracted envelope. (bottom) Envelope correlation matrix for sols 237-239 between the vertical ground acceleration and pressure for frequencies 0.01 Hz up to Nyquist for each sensor's data rate acquisition, taken in logarithmic frequency intervals. The mean correlation coefficient across the VBB Z frequency is shown above the matrix, while for the pressure frequency the mean values are shown to its right.

⁵⁷⁶   Fig. 6 shows the correlation between the environmental and seismic signals, over the full
⁵⁷⁷ bandwidth for wind and as a function of frequency as a correlation matrix for the pressure.
⁵⁷⁸ The broadband noise injection induced by the atmosphere is correlated with the wind (top
⁵⁷⁹ row) and within and across frequencies for the pressure and acceleration envelopes. The
⁵⁸⁰ correlation coefficient matrix can be regarded as an estimate of the cross-frequency power
⁵⁸¹ comodulation. This matrix is calculated as the correlation coefficient for the variation of
⁵⁸² spectral power in each overlapping frequency band of logarithmic spacing, between 0.01-10
⁵⁸³ Hz for the VBB Z and 0.01-4 Hz for the pressure. The wind is already in the appropriate
⁵⁸⁴ domain for comparison, and the correlation to wind against the other two variables is shown
⁵⁸⁵ at the top row. This establishes that cross-frequency power variations are comodulating

from the interactions by the atmosphere and ground acceleration. Whereas comodulation breaks down below 0.1 Hz in the ground acceleration due to multiple glitches in these long period windows, the pressure to wind relationship is maintained.

These atmosphere-seismic relationships were illustrated in detail in Section 4.3.1, where Fig. 3 showed that the pressure envelopes exhibits a similar correlation to the seismic acceleration envelope as wind speed. In Fig. 3b the wind speed is plotted against the pressure envelope for multiple increasing bands, 0.01-0.1 Hz, 0.1-0.5 Hz, 0.5-1 Hz and 1-4 Hz. It can be seen that for > 0.5 Hz, above a $2.4\,\mathrm{m\,s^{-1}}$ threshold for sols 237–239, these relationships correlate with a single linear relationship $a = 1$, while the exponent a becomes increasingly larger at lower frequencies. The increased spread observed at lower frequencies is also reflected by the slightly lower correlation coefficient reported by the top row of Fig. 6. We investigated this relationship across multiple seasons and found a similar correlation.

As a result, we can see that the pressure envelope provides similar information to the wind speed above the seasonal variable wind speed threshold. The pressure sensor is designed to observe static pressure up to a sampling rate of 20 samples per second and so it is shielded by an inlet designed to transmit only the static component (Banfield et al., 2018). In Banfield et al. (2020) it was suggested that the pressure sensor may be sensitive to wind at higher frequencies due to reduced efficiency of the inlet shielding mixing a proportion of the dynamic pressure into the measurement which would then be indistinguishable from high frequency static pressure. Moreover, static pressure and wind speed will be correlated through turbulence inducing static pressure variations (Spiga et al., 2020). A precise uncoupling of these factors is beyond the scope of this work.
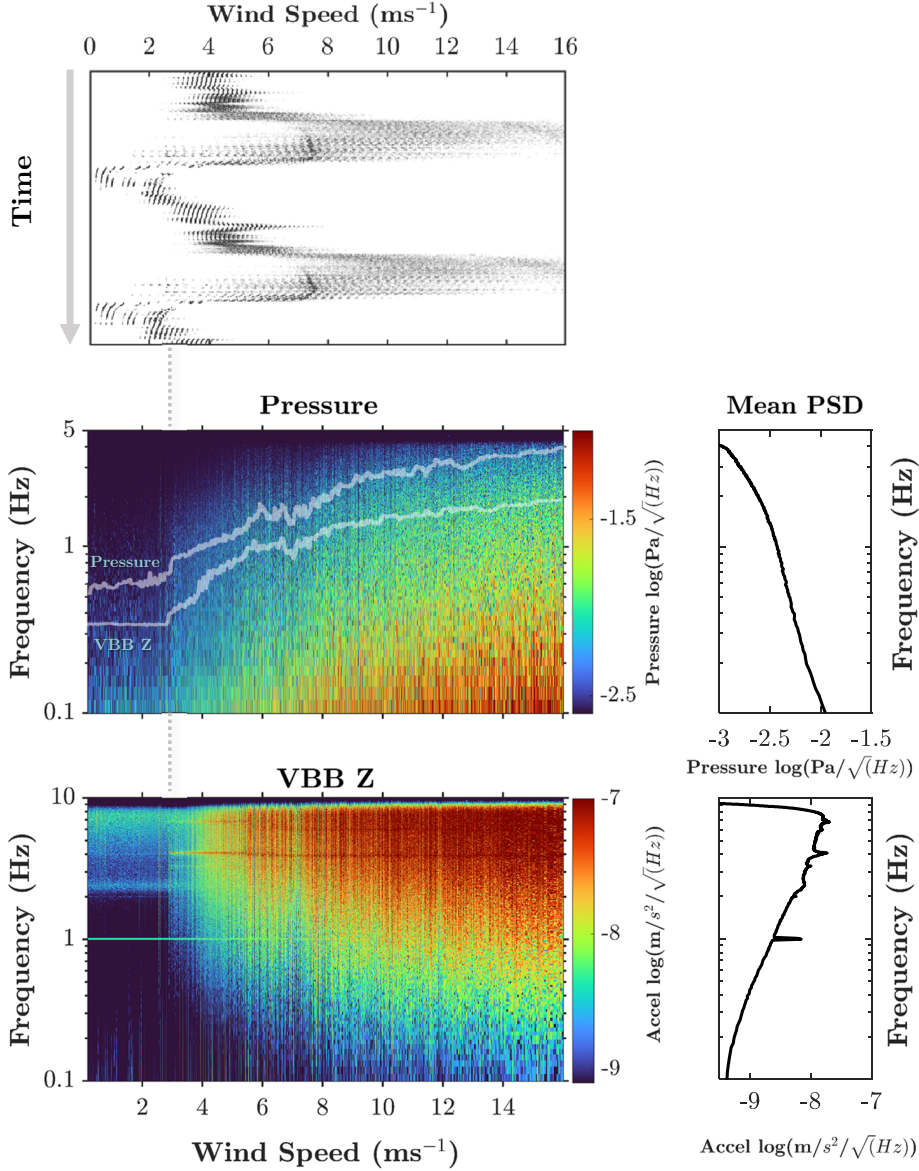
Figure 7: Investigation of the wind speed threshold (top) Wind Speed time-series for sols 361–362. (middle) Histograms of the wind speed per frequency bin of pressure and (bottom) vertical ground acceleration. The overlain transparent grey line is the logarithm of the integral for the total spectral amplitude over all frequencies shown, plotted on an arbitrary axis for visual comparison of features such as the wind speed threshold and a further corner point a $7\,\mathrm{m\,s^{-1}}$. The mean power spectral density is plotted on the right for both pressure and VBB Z.

Through both instrumental constraints and turbulence joint modulation of the pressure and wind data can be expected to reflect the dynamic pressure generating forcing on the lander or the WTS which couples through the regolith to the SEIS assembly. In Section 4.1 we outline how the dynamic pressure will drive the observed seismic response through drag forcing. As discussed these equations are in turn dependent on a myriad of factors (e.g. wind Reynolds number, atmospheric density changes due to seasonal and diurnal pressure and temperature changes,surface area via a wind direction dependence and regolith

response) which would give rise to an array of sensitivities for different atmospheric conditions, including mechanisms dependent on the detailed geometry of the lander such as vortex shedding.

We now discuss the wind speed threshold below which SEIS acceleration no longer clearly correlates with the wind speed and often reaches the noise floor in several bandwidths. This is the quiet period regime in which most seismic event identifications have been made. In Lognonné et al. (2020) it was stated that this wind speed corresponds to a drop in Reynolds number, decreasing the resultant injection. In addition, wind speed retrieval also becomes more difficult and so exact values should be interpreted with caution (Banfield et al., 2020). Although the wind speed can be reliably assumed to vary below this threshold at this period, its occurring fluctuations cannot be reliably quantified. Fig. 7 visualizes the threshold for sols 361–362 by comparing the VBB vertical acceleration component to the pressure frequency histogram using pressure as a proxy for wind over an increased bandwidth due to their observed comodulation. The threshold is indicated by the dividing grey dashed line at $2.8\,\mathrm{m\,s^{-1}}$ for these two early summer sols, a cut-off point that differentiates the response in the behaviour for both pressure and VBB, at all frequencies. It is noticeable that the lander resonances also diminish in power at this point, falling below the instrument noise floor with an abruptness that is not seen in the ambient broadband signal. This could be associated with the collapse of the daytime turbulence which provides excitation of the lander modes. This figure further illustrates the joint broadband nature of the environmental injection for energy across the 0.1 to 10 Hz bandwidth with the energy across all bandwidths correlated between the pressure and seismic signals.

The overlain transparent grey line on the 2-D histograms of Fig. 7 is the logarithm of the total power showing the comodulation of the seismic signal power and wind strength during the two-sol observation time. For the VBB this is dominated by the higher frequencies due to the sensor's response and the excitation of mechanical modes observed at > 1 Hz which concentrate excess power, as indicated by the mean PSD in Fig. 7. For the pressure, this would be dominated solely by a reverse response in the pressure sensor compared to the VBB, with no modes present. Notice the co-occurrence of the wind speed threshold, flattening this integral at $2.8\,\mathrm{m\,s^{-1}}$. Above this threshold the increase in the summed power behaves differently for the two sensors. This increases linearly for the pressure in line with the relationships in Fig. 3. In contrast, the increase above this threshold for the vertical acceleration is a steep power-law with an exponent close to $a = 4$ (see Fig. 5) up to $\sim 7\,\mathrm{m\,s^{-1}}$, Both sensors capture a break-point at this wind speed of $\sim 7\,\mathrm{m\,s^{-1}}$, a value which here signifies the transition from the night-time low-level jet to the turbulent daytime after sunrise, to the transition after the turbulence after sunset. Above this break-point, the seismic acceleration transitions into a power law with an exponent closer to $a = 2$.

4.3.4 *Predicting the wind speed and direction*

Fig. 8 exploits the cross-frequency coupling investigated earlier in Fig. 6 of the wind to both the ground acceleration and pressure as a potential proxy for wind speed. The energy is extracted in 1-Hz narrow frequency bands, starting from 0.1 Hz up to 8 Hz for the VBB and 4 Hz for pressure to avoid anti-aliasing effects. The square root of the envelope of each incremental band is moment matched to the global moments of the wind over the 3-sol period, sols 237–239. Due to the consistent broadband characteristics of the noise induced by the atmosphere, both pressure and acceleration indicate that any frequency band is directly coupled to any other frequency band between pressure and VBB, at all times. This can be also realized by the good overlap of these scaled relationships, providing predictions with minor differences. Therefore, the energy content of both pressure and ground acceleration exhibits the same behaviour and are good predictors of the wind. This is shown by the close linearity in the performance of the predictions against measured wind speeds in the middle plots of Fig. 8a & b.
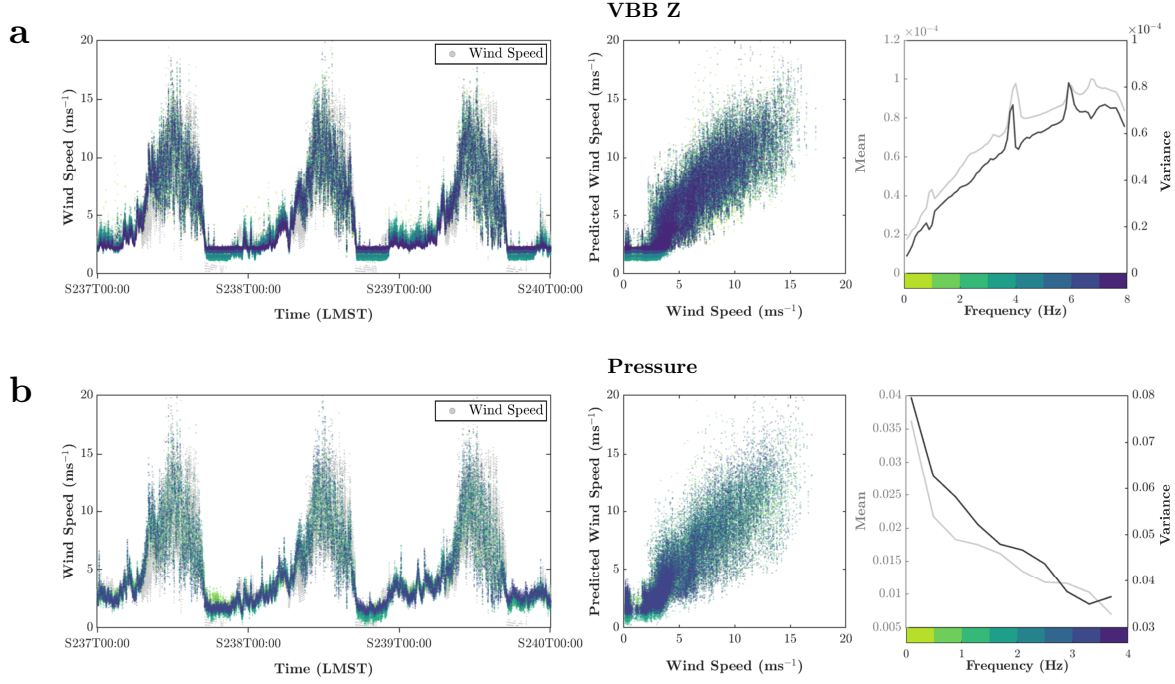
Figure 8: a - (Left) Wind Prediction from Z acceleration in incremental bands of 1 Hz, from 0.1 Hz to 8 Hz and colour-coded for each band. For each frequency band, we match its first two moments to the wind moments. Notice how they all overlap, providing predictions with minor differences (Middle) VBB Z prediction of wind vs actual measured. (right) The evolution of the mean and variance of VBB Z acceleration, with each data point representing the moments in 0.2 Hz bands. Note the increase in the mean and variance at the resonant modes. b - (Left) Wind Prediction solely from the pressure measurements in incremental bands of 1 Hz, from 0.1 Hz to 4 Hz. Each frequency band is matched to the wind moments, colour-coded (Middle) The relationship between the predicted wind vs actual measured. (right) The evolution of the mean and variance of the pressure

On the right hand side of Fig. 8a & b, the evolution of the mean and variance in incremental frequency bands of 0.2 Hz is shown for both pressure and vertical ground acceleration. The mean and variance of the pressure drops with increasing frequency, while it increases for VBB. This is in line with the expected noise curves of the two systems (Banfield et al., 2018; Lognonné et al., 2019). For SEIS, notice the synchronized variations between the mean and variance at the resonant modes of 4 Hz, 6 Hz and 7 Hz, tick noise 1 Hz and 2.4 Hz mode. The diurnal temperature variation causes a shift in the frequency of a subset of the mechanical modes. Therefore, the variance will be higher within the frequency range encompassing these lander modes since they vary diurnally. On the contrary, the persistence of a constant amplitude tick noise in the quiet and intermediate regimes identified earlier in Section 4.3.1, promotes an inverse relationship with less variance and a higher mean. These modes therefore provide a good representation of the lander's diurnally evolving state and can also be used as a proxy of the excitation induced by the atmosphere.

We have also successfully established a prediction of the measured wind direction by TWINS from the seismic energies of the horizontal components. The measured wind direction by TWINS is determined by a combination of the measurements of the sensors and computational fluid dynamics of the lander disturbances by the wind flow (Banfield et al., 2020). Our approach exploits the acceleration induced by ground deformations from the lander to estimate the direction of forcing on the lander from the wind. We have estimated

this by moment-matching with a single mean and variance from the inverse tangent function of the horizontal acceleration envelopes of the VBB components E and N, band-passed between 0.5-1 Hz. The agreement between the VBB prediction and the actual wind direction partly breaks down at the onset of the sun setting, during the steep temperature gradient observed right before the sunset (see Fig. 2) and through the late afternoon's quiet period. This corresponds to the lack of environmental injection which induces mechanical vibrations and falls steeply below the wind threshold (Fig. 7). This period also occurs at the wind speed threshold observed by both the pressure and VBB sensors. Our method therefore provides an independent confirmation of the atmospheric diurnal cycle, synoptic (day-to-day) variations and seasonal cycle of wind direction and wind speed retrieved by TWINS. These predictions offer an alternative means of redundancy in maintaining observations of the atmospheric variables, both for short and longer time-scales.
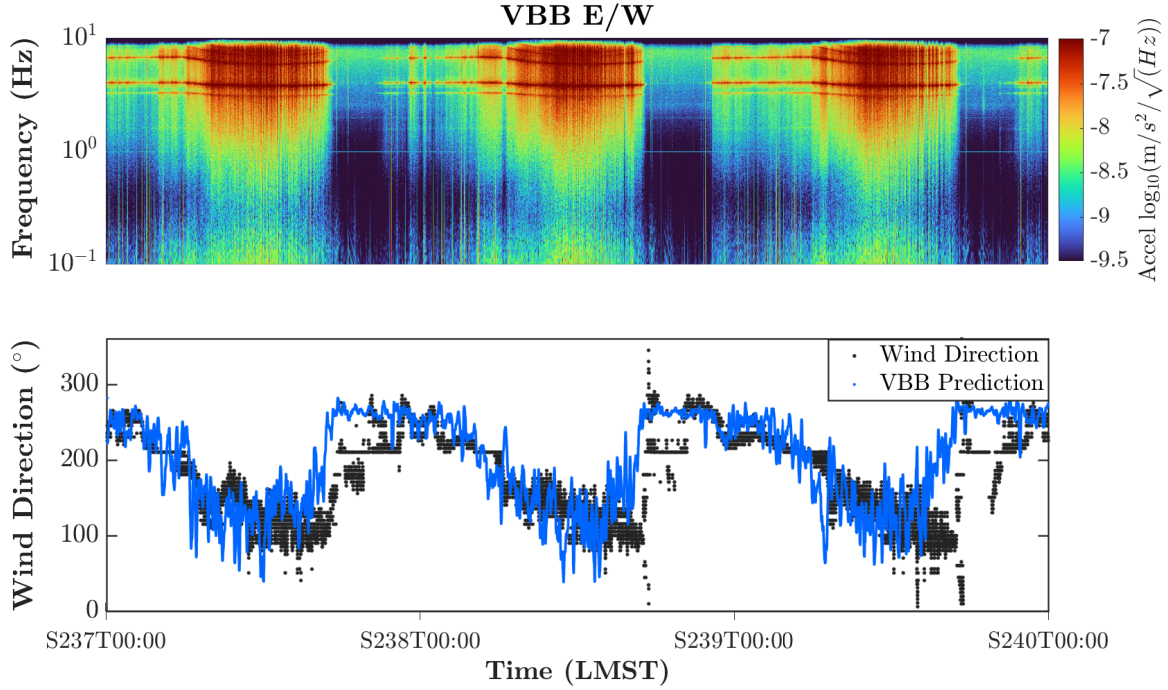
Figure 9: The wind direction estimated from the inverse tangent function of the horizontal acceleration envelopes of the VBB components E and N. The frequency band used here is 0.5 - 1 Hz. The wind direction predicted by the VBB indicates a disagreement in the Martian afternoon, a period during which the wind speed is below the threshold of $2.8\,\mathrm{m\,s^{-1}}$ for reliable wind speed and direction retrieval, but also a time during which there are minimal lander vibrations.

4.4 Discussion on Observed Environmental Sensitivity

In this Section we have examined the comodulation of the seismic ground motion with respect to the pressure and wind data. The aim is to determine the extent at which the observed SEIS data is contaminated by environmental induced signals. The seismic acceleration envelope correlates with the pressure envelope and wind speed. These correlations follow a set of power-law defined regimes which change in occurrence and sensitivity across seasons. Furthermore, we have analysed the correlation between the pressure and wind

data in order to understand the core factors of the observed comodulation. Here, we will summarize the underlying mechanisms for such observed relationships.

As already stated the main injection pathway is through the dynamic pressure, proportional to U^2, which induces a forcing described by the drag equation (Murdoch et al., 2017). These forces are applied predominantly to the lander but also to other site components such as the WTS and the tether. This forcing then produces ground deformation which couples to the SEIS assembly (Mimoun et al., 2017). Such forcing can also be directly applied to the regolith producing a tilt and requires consideration of the wind direction and air density. On top of this direct wind-induced forcing, other coupling mechanisms can be considered such as injection from a pressure field advected by the wind (G. G. Sorrells, 1971). It must be considered that at different times different mechanisms may dominate.

Over the course of a sol, three regimes are generally observed in terms of the relationship between the seismic and environmental signals: (i) a shallow power law with exponent near 2 during the daytime convective turbulence, (ii) a steep power-law with exponent near 4 during the nighttime through morning nocturnal low-level jet and (iii) a quiet period where the wind speed drops below a threshold (in the Reynolds number) where no seismic response is observed. These regimes have been observed to vary across seasons and are weather dependent. For example, we saw that only the steeper power-law is observed on sols 98–99. For the other sols, we've observed that daytime is maintained in the shallower power-law, with an intercept value that shifts negatively, in-line with changes in density. At least one example, sols 361–362, indicates a correlation to the wind speed direction at sunrise, where a prominent divergent branch in the relationship merges the nighttime to the daytime regime.

The comodulation approach has enabled this quantification without a full development of a theoretical model for each injection pathway. As stated these pathways are numerous and have complex dependencies. For example the drag coefficient depends on the Reynolds number which, in turn, depends on wind speed, air viscosity and density. This dependence can account for several diurnal and seasonal patterns. For example, the slow decrease in sensitivity of the daytime turbulence regime can be attributed to such a factor. On a seasonal scale, the air density on Mars can change by 30% over a year, with a diurnal density varying by 50%, between daytime and nighttime. This not only causes a change in sensitivity but may also cause the observed variation in the cut-off threshold which changes between 2-$2.8\,\mathrm{m\,s^{-1}}$. Different atmospheric properties and weather patterns do induce some of the variation observed. On top of the variation in the initial forcing, they may also influence the coupling mechanisms. The InSight lander and deployed SEIS stand atop a poorly sorted, thin layer of unconsolidated sand that is underlain by a cemented fine-grain matrix, called duricrust, that is of cm-variable thickness (Golombek et al., 2020). Beneath this layer, the regolith consists of buried rocks from impact ejecta with a distribution that increases in size with depth (Charalambous, n.d.). Consider how this near-surface stratigraphy of the regolith and the lander itself are subject to steep temperature gradients. As a result, their thermoelastic properties are affected, as seen in the diurnal variation of the lander resonances with some appearing and disappearing on a seasonal scale. On top of this, radiative temperature effects on the lander may also impact TWINS winds retrieval. Further analysis complemented by surface brightness temperature sensing (Mueller et al., 2020) and air temperatures may provide a deeper insight to the properties of the Martian regolith deformation and lander dynamics. We consider that the comodulation approach has short circuited the requirement for this full model but posit that these theoretical aspects are encompassed in the observed variation. The precise quantification of this physics is the subject of further work.

Our comodulation method can be further exploited to provide the resolution which TWINS lack during the passage of convective vortices. Charalambous et al. (2020) identified wind retrieval issues due to perturbations and die saturation from high vorticity conditions during convective vortex encounters. Our method can provide continuous wind predictions

and therefore provide estimates of wind peak speeds to fill in the missing wind data during such turbulent conditions. This may allow estimations of high-frequency wind speeds that have never been resolved before, to better identify the sudden peaks in the wind speed and infer the fluid threshold for the onset of particle detachment from the surface, for both sand motion and dust lifting (Charalambous et al., 2020). This will provide an insight into the long-standing paradox of aeolian transportation and the mechanistic relationships in the coupling between atmospheric processes and the surface of Mars.

5 Environmental injection analysis for seismic events

The InSight mission includes the Marsquake Service (MQS) who sift through the data to identify events as part of mission operations, with nearly 400 such events identified in the current catalogue V2 (Giardini et al., 2020; InSight Marsquake Service, 2020). The understanding of the injection of environmental sources into seismic data is key for the identification and analysis of seismic events. This is especially true in light of the Viking mission (Anderson et al., 1977; Lorenz et al., 2017), and the key level 1 science goals of this mission are dependent on the identification of seismic events in the downlinked data (Lognonné et al., 2019; W. Banerdt et al., 2013).

In this section, we extend the comodulation approach to predict the energy injection into the seismic band of interest from the wind and pressure signals, and then compare this to the observed event to obtain a signal to noise ratio (SNR). The initial SNR and quality metrics so far implemented by the MQS are based on the amplitude of the seismic signal and its separation from the signal background. On the other hand, the proposed comodulation-based SNR incorporates the independence of the event from environmental sources providing a new dimension for analysis. Specifically, the aim is to quantify the divergence of the seismic signal from that expected from environmental forcing. This divergence can be expressed as the SNR of any event under analysis, the ratio of excess seismic energy compared to that expected from environmental injection, that is our proposed comodulation-based SNR is in the energy domain.

5.1 Moving moment matching for envelope prediction

In order to implement our comodulation approach to provide an SNR metric, we must develop a regression between the envelopes obtained in Section 4.2. The method of moments has already been introduced for this task in Section 4.2.1, which we have used to compare the wind speed, seismic and pressure envelopes within distinct power-law regimes in Section 4.3.1. The method of moments is an estimation method, which matches the population moments (up to second-order in our case) of two time series. This is a regression, where the moments of a time series are matched to the reference. Although matching within each power-law regime is suitable for a sensitivity comparison, it can be seen that the variance and mean of wind speed, pressure and seismic acceleration is not constant throughout each regime, that is, each envelope time series exhibits unconditional heteroskedasticity, i.e. it features non-constant variances at different times (Bollerslev, 1986). For forecasting equations, e.g. in equity markets (Engle & Sokalska, 2012), heteroskedasticity imposes a serious challenge due to unpredictable variance measures. However, identifying strong evidence of seasonal or diurnal components, determines heteroskedasticity to unconditional (Bollerslev et al., 1992).

In our case, heteroskedasticity could rise mainly from the identified changes in atmospheric conditions in Section 4.4. For example, air density variation throughout the convective turbulence daytime regime or wind direction reversals. To this end, a finer grained approach is required to assess environmental injection into a potential marsquake, which also vary over a smaller scale than these regimes and have typical durations ranging from 5–30

minutes. Instead, the moment matching is extended to operate over a sliding window, thus enabling an adaptive regression where the estimation is locally linear, akin to a manifold. This proposed moving-moment-matching procedure captures the variation in the mean and variance over time in order to create a smooth prediction which adequately represents the current evolving conditions observed throughout the Martian day.

To calculate the proposed prediction, consider the moving average filter defined as the operation

$$\text{MMean}(e[t], K, L) = \frac{1}{K+L} \sum_{n=t-K}^{t+L} e[t] \tag{5}$$

which outputs the mean value of the input $e[t]$ over K time steps before and L following time steps. Next we define the moving variance operation

$$\text{MVar}(e[t], K, L) = \frac{1}{K+L-1} \sum_{n=t-K}^{t+L} |e[n] - \text{MovMean}(e[t], K, L)|^2 \tag{6}$$

which similarly outputs the variance of the input $e[t]$ over K time steps before and L following time steps.

Using these operations, the moment matching in Equation 2 is then done on a sliding basis, where the matched time series $e_Y^{MM}[t]$ at step t of the input time series $e_Y[t]$ is matched to the same variance and mean as the time series $e_X[t]$ for the preceding K and following L steps. This process is outlined in Algorithm 1. The moment matching is done in the logarithmic domain, as the relationships identified in Section 4.3 are described through power-laws. Let e_Y denote the wind speed or pressure energy and e_X the seismic energy, the algorithm yields a regression where the output $e_Y^{MM}[t]$ is the prediction of the seismic energy at time step t from the atmospheric variable. The variable σ can be set to remove outliers from the sample moments calculation, with steps 5 to 9 of the algorithm detecting if the moving standard deviation of either $e_X[t]$ or $e_Y[t]$ is over the threshold σ, with the corresponding samples removed from subsequent calculation. In this way, momentary extrema do not bias the matching.

Algorithm 1 Moving moment matching

1: **Input:** $e_X[t]$ **and** $e_Y[t]$ **for** $t = 1, 2, \ldots, N$, K, L, σ
2: **for** $t = K, K+1\ldots, N$ **do**
3: $\quad SD_X[t] = \exp((e_X[t] - \text{MMean}(\log(e_X[t]), K, L))\text{MVar}(\log(e_X[t]), K, L)^{-\frac{1}{2}})$
4: $\quad SD_Y[t] = \exp((e_Y[t] - \text{MMean}(\log(e_Y[t]), K, L))\text{MVar}(\log(e_Y[t]), K, L)^{-\frac{1}{2}})$
5: $\quad$ **if** $SD_X[t] > \sigma$ **then**
6: $\quad\quad e_{Xn}[t] = NaN$
7: $\quad$ **end if**
8: $\quad$ **if** $SD_Y[t] > \sigma$ **then**
9: $\quad\quad e_{Yn}[t] = NaN$
10: $\quad$ **end if**
11: **end for**
12: **for** $t = K, K+1\ldots, N$ **do**
13: $\quad e_Y^{MM}[t] = (\log(e_Y[t]) - \text{MMean}(\log(e_{Yn}[t]), K, L))\left(\frac{\text{MVar}(\log(e_{Xn}[t]), K, L)}{\text{MVar}(\log(e_{Yn}[t]), K, L)}\right)^{\frac{1}{2}} + \text{MMean}(\log(e_{Xn}[t]), K, L)$
14: **end for**

Sol 189

Time Series	Spectrograms	Match Moments
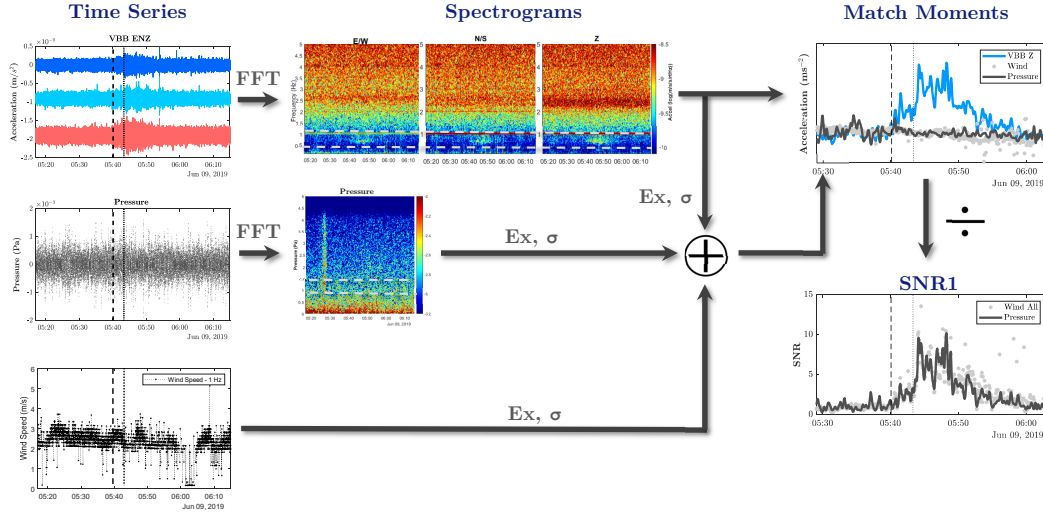
Figure 10: A diagram illustrating the steps of the environmental independence SNR algorithm. The pressure and seismic acceleration time series are first transformed to a spectrogram and the envelopes obtained as in Section 4.2. The mean Ex and standard deviation σ are extracted from the seismic acceleration envelope, pressure envelope and wind speed in order to perform a regression through moment matching. The ratio of the resulting matched envelopes then yields an SNR.

5.2 An SNR metric for seismic events

This regression is used to estimate the independence of the observed seismic signal from the weather and so obtain an SNR for the events in the seismic catalogue.

The first proposed metric to compare two events is the ratio of the instantaneous energy given as

$$\text{SNR1}[t] = \exp(2(\log(e[t]) - e_Y^{MM}[t])), \tag{7}$$

where $e[t]$ and $e_Y^{MM}[t]$ are obtained from Algorithm 1. The peak value of $SNR1[t]$ during an event is then the SNR estimate. The SNR time series $SNR1[t]$ is then averaged as

$$\text{SNR2}[t] = \text{MMean}(SNR1[t], K, L). \tag{8}$$

The peak value of SNR2$[t]$ during the event then yields a second metric. This second metric acts to average over an event and thus avoid instantaneous features and better assess the overall power injection. However, the averaging may bias the result if there is an extremely large divergence. For a given event this is reported for both regressions to wind and pressure and the full process is summarised by Algorithm 2.

5.2.1 An application of the SNR analysis to recorded marsquakes

The MQS identify and maintain a catalogue of all seismic events in the InSight data. The aim is to catalogue and classify all suspicious signals and indicate their quality and usability for seismic analysis. In this section we apply our proposed SNR metrics to a set of marsquakes identified so far. In doing so we show how our comodulation analysis identifies

---

Algorithm 2 SNR calculation for seismic events

1: Obtain seismic trace $x[t]$ and wind speed/pressure trace $y[t]$ for at least $8000\,\text{s}$ before and after the event.
2: Calculate the spectrogram of the seismic signal $Y[l,t]$ for a window size W_{len}, window overlap OL_{win}, number of PSD averages N_{av} and PSD window overlap OL_{PSD}.
3: Calculate the envelope $e_X[t]$ for frequency bins corresponding to the event bandwidth $f_{min} - f_{max}$ using (1).
4: **if** Seismic to pressure SNR **then**
5:     Calculate the spectrogram of the pressure signal $Y[l,t]$ for a window size W_{len}, window overlap OL_{win}, number of PSD averages N_{av} and PSD window overlap OL_{PSD}.
6:     Calculate the envelope $e_Y[t]$ for the full pressure bandwidth using (1).
7: **else** Seismic to wind speed SNR
8:     Use the wind speed as the envelope, $e_Y[t] = y[t]$.
9: **end if**
10: Calculate the moving moment matched pressure/wind speed envelope using Algorithm 1 using the obtained $e_X[t]$, $e_Y[t]$ for a given K_{MM}, L_{MM} and σ.
11: Calculate the instantaneous SNR, SNR1$[t]$, using (7).
12: Calculate the averaged SNR, SNR2$[t]$, using (8) and K_{SNR} L_{SNR}.
13: Find the peak value of SNR1$[t]$ and SNR2$[t]$ during the event time as SNR1 and SNR2.

---

the divergence in the seismic acceleration envelope from the wind speed and pressure envelope, which is then quantified by the proposed SNR metrics. This is extremely useful in light of the fact that, envelope alignment and analysis has so far been particularly fruitful for the interpretation of what InSight has observed in terms of the structure of Mars (Giardini et al., 2020; Lognonné et al., 2020).

The events identified by the MQS have been categorised into the following types:

1. Low frequency (LF) - energy below $2.4\,\text{Hz}$.
2. Broadband (BB) - energy mostly below $2.4\,\text{Hz}$ with some slight excitation above.
3. $2.4\,\text{Hz}$, and event with energy solely around the ambient resonance which is proposed to be of a potentially geophysical origin (Lognonné et al., 2020).
4. High frequency (HF) - energy centred around and above $2.4\,\text{Hz}$, considered to be larger versions of the $2.4\,\text{Hz}$ events.
5. Very high frequency (VF) - energy increasing with frequency in the horizontal components often exciting the $2.4\,\text{Hz}$ resonance.

For more details of these events see (Giardini et al., 2020). The Algorithm 2 was implemented for for a set of these events with the following parameters:

1. Event bandwidth $f_{min} - f_{max}$ in Table 1.
2. Window length $W_{len} = 50\,\text{s}$ and overlap $OL_{win} = 90\%$ between spectrogram slices.
3. Spectrogram slice PSD number of averages $N_{av} = 2$
4. Length of moving moment matching $K_{MM} = 1000\,\text{s}$ and $L_{MM} = 0$ for longer period LF/BB events and $K_{MM} = 500\,\text{s}$ and $L_{MM} = 0$ for the HF/VF/$2.4\,\text{Hz}$ events
5. Number of standard deviations to exclude from moment calculation $\sigma = 5$.
6. Length of SNR averaging $K_{SNR} = 500\,\text{s}$ and $L_{SNR} = 500\,\text{s}$.

Figure 11 shows the spectrogram, matched envelopes and SNR metrics for the events S0173a, S0235b, S0185a and S0128a. The S0173a and S0235b events are the two category A events observed so far (Giardini et al., 2020). From the examination of the matched envelopes, both show a clear divergence of the seismic energy from the wind and pressure.

The power of the moment matching for event analysis is well demonstrated by S0173a as it occurs during a noisy period and so the envelopes track well until the event where the SNR metrics are able to be obtained. The transient spikes in the SNR1 values are due to VBB sensor glitches (Scholz, J.-R. et al., 2020). On the other hand, the S0235b event highlights the data dependency issues of this metric. At the beginning of the time-window demonstrated at approximately 11:20, a broadband high amplitude signal indicates a mechanical recentering process of one of the VBB components, with a clear divergence to the atmospheric noise. About 10 minutes prior to the event onset, the wind speed drops very low and this divergence is captured by both the wind and pressure SNRs. In fact, the wind SNR2 is seen to become biased for the surrounding samples, leading to an overestimation. Here, the wind speed has actually dropped below the wind speed threshold of $2.4\,\mathrm{m\,s^{-1}}$ discussed in Section 4.3. For a true determination, the parameters K_{MM}, L_{MM}, K_{SNR} and L_{SNR} must be adjusted. To show this adjustment consider event S0128a in the fourth column. For such VF and higher frequency events we choose a shorter moment matching window of $K_{MM} = 500\,\mathrm{s}$ in order to capture the faster variation in the bandwidth, owing to its higher sensitivity observed in Section 4.3. Note that this envelope is calculated on the north component, as for the higher frequency events the horizontal power is greater (Giardini et al., 2020). The selection of the window length is critical in our SNR estimation; too short duration and the algorithm risks overfitting, whereas a long enough window risks contaminating the statistics of different regimes observed throughout the Martian sol introducing back heteroskedasticity. Therefore these selected window lengths provide the best SNR calculations without any risk of overfitting or regime contamination.

Now consider the event S0185a in the third column of Figure 11. This is a relatively low amplitude signal, however, with our analysis its separation is clear and it receives a relatively high SNR. This indicates that there is little corruption of the data by environmental injection and so any estimated parameters from this event would be relatively reliable with respect to its strength. This shows the power of out approach to indicate a level of confidence in derived interpretations.

The proposed SNR metrics are based on the measured data and therefore they rely on good data quality in all data. For example, consider the above discussion for S0235b. These data issues include:

1. Glitches in either the seismic, wind speed or pressure data. These corrupt both moments, the mean and variance, in the statistics within an event and inject power to the signal, leading to an incorrect SNR determination. These glitches are prevalent in S0173a in Fig. 11

2. Drop out/missing data, which renders an assessment impossible.

3. Very low amplitudes (i.e. low wind speed), which causes an instability in obtaining a result (e.g. S0235b in Figure 11). This often occurs when the wind speed drops below the threshold and so interpretation of these values should be cautious. In addition, wind retrieval issues often result in no data points during which the algorithm depends on interpolated values.

Figures 12 show the moving matched moment envelopes for a selection of key LF/BB and HF/VF events as identified in (Giardini et al., 2020) with the SNRs given in Table 1. The event bandwidths f_{min} and f_{max}, manually optimised for each event, are also provided in Table 1.

The key value of this measure is that it indicates the independence as opposed to simply strength of the seismic signal. On top of the SNR value, the moving moment matching regression yields the ability to assess correlation of the envelopes. For the largest events, while they are already clear, this analysis can show the degree to which portion of an event is independent. For smaller events, this metric may more appropriately represent their significance. For example, event S0189a is a low energy event with a relatively higher SNR

from our analysis than from the amplitude-based MQS SNR. The divergence can be best
seen as the envelope does not correlate with the pressure envelope or wind speed. On the
other hand, an event which exhibits some correlation with the pressure envelope or wind
speed and so interpretation must take into account a potential injection, for example S0167a
in Fig. 12.
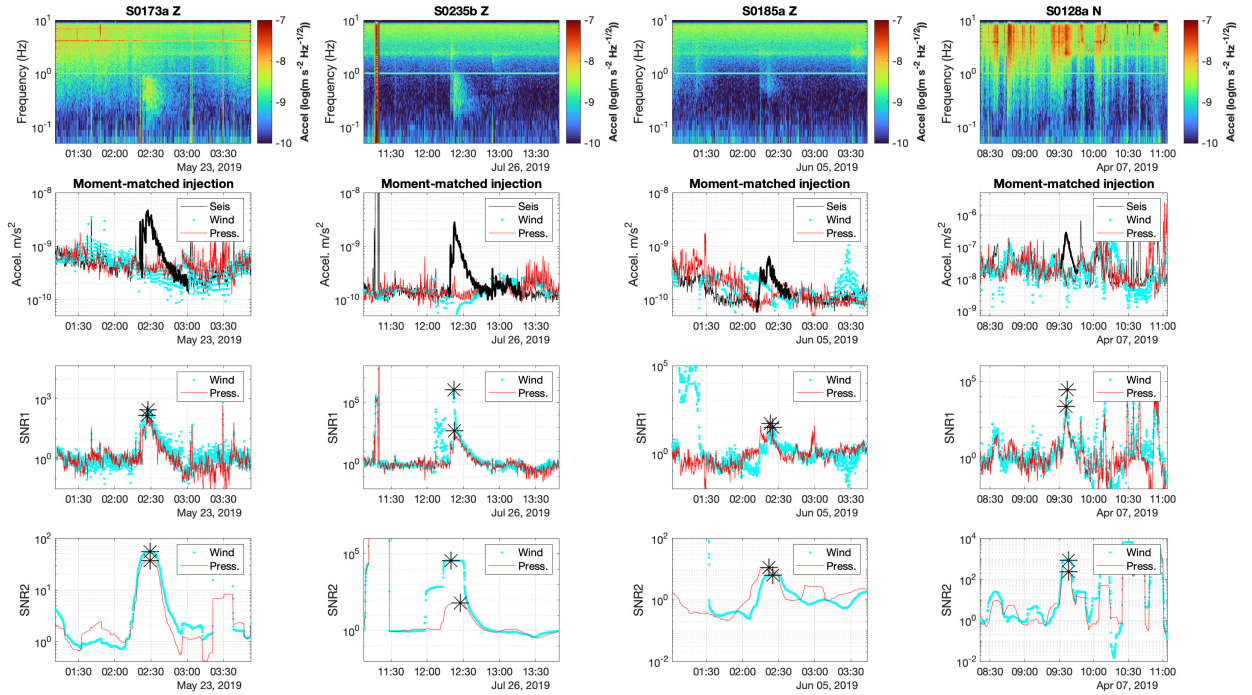
Figure 11: The derivation of the SNR metrics for selection of quality A LF (S0173a) and
BB (S0235b) and quality B VF (S0128a) and LF (S0185a) events. The top row panels show
the vertical (Z) spectrogram of event (except S0128a, showing north (N)), second row the
seismic envelope (black, event period from InSight Marsquake Service (2020) highlighted
with thick line) and moving moment matched wind (cyan) and pressure (red), third row the
SNR1 metric (7) for wind and pressure and the fourth row the SNR2 metric (8). The black
stars refer to the peak picked for the SNR metrics. Note that in many of these events the
wind speed drops below the threshold discussed in Section 4.3.
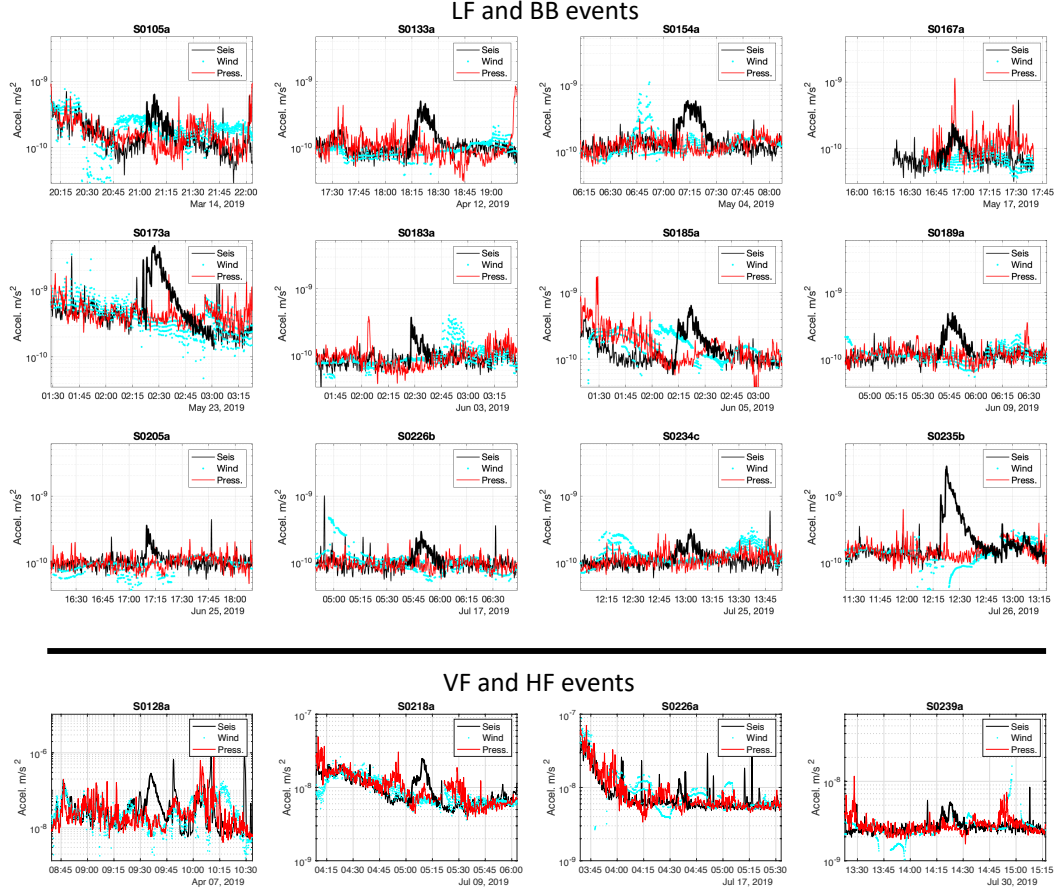
Figure 12: A set of moving moment matched envelopes for important LF, BB, HF and VF events as highlighted in (Giardini et al., 2020).

Event Name	Bandwidth	MQS SNR	Mean Wind m/s	SNR2 Wind	SNR2 Press.
LF/BB					
S0105a	$f_{min} = 0.31\,\mathrm{Hz}$ $f_{max} = 0.5\,\mathrm{Hz}$	8.10	2.48	2.65	10.79
S0133a	$f_{min} = 0.31\,\mathrm{Hz}$ $f_{max} = 0.5\,\mathrm{Hz}$	4.80	1.75	-	8.50
S0154a	$f_{min} = 0.33\,\mathrm{Hz}$ $f_{max} = 0.67\,\mathrm{Hz}$	19.80	2.46	9.24	11.95
S0167a	$f_{min} = 0.17\,\mathrm{Hz}$ $f_{max} = 0.67\,\mathrm{Hz}$	8.50	2.58	4.09	1.64
S0173a	$f_{min} = 0.18\,\mathrm{Hz}$ $f_{max} = 0.48\,\mathrm{Hz}$	84.10	3.30	55.24	37.18
S0183a	$f_{min} = 0.2\,\mathrm{Hz}$ $f_{max} = 0.67\,\mathrm{Hz}$	3.20	2.24	2.81	4.76
S0185a	$f_{min} = 0.33\,\mathrm{Hz}$ $f_{max} = 0.66\,\mathrm{Hz}$	4.80	2.31	6.32	11.28
S0189a	$f_{min} = 0.28\,\mathrm{Hz}$ $f_{max} = 0.83\,\mathrm{Hz}$	1.30	2.48	7.91	6.94
S0205a	$f_{min} = 0.36\,\mathrm{Hz}$ $f_{max} = 0.83\,\mathrm{Hz}$	2.00	1.93	-	3.29
S0226b	$f_{min} = 0.29\,\mathrm{Hz}$ $f_{max} = 0.83\,\mathrm{Hz}$	3.30	1.20	4.17	3.20
S0234c	$f_{min} = 0.33\,\mathrm{Hz}$ $f_{max} = 0.83\,\mathrm{Hz}$	0.70	1.87	2.86	3.48
S0235b	$f_{min} = 0.15\,\mathrm{Hz}$ $f_{max} = 0.91\,\mathrm{Hz}$	290.50	0.78	-	84.00
VF/HF					
S0128a	$f_{min} = 3\,\mathrm{Hz}$ $f_{max} = 7.5\,\mathrm{Hz}$	7.10	4.53	433.16	120.09
S0218a	$f_{min} = 5\,\mathrm{Hz}$ $f_{max} = 7.5\,\mathrm{Hz}$	5.00	3.09	4.07	3.21
S0226a	$f_{min} = 3\,\mathrm{Hz}$ $f_{max} = 7.5\,\mathrm{Hz}$	3.10	0.26	1.97	1.53
S0239a	$f_{min} = 3\,\mathrm{Hz}$ $f_{max} = 5\,\mathrm{Hz}$	4.80	0.34	0.80	1.91

Table 1: SNR Table for significant events (Giardini et al., 2020) shown in Fig. 12

5.2.2 Operational aspects of the SNR metrics

The MQS catalogue contains an SNR calculated based on the ratio of the power (obtained from the PSD) in the event bandwidth during and just prior to the event (Giardini et al., 2020). The bandwidth is selected depending on the event type (i) for the LF and BB the power is calculated for $f_{min} = 0.2\,\text{Hz}$ and $f_{max} = 0.5\,\text{Hz}$ and (ii) for the HF, VF and 2.4 Hz events the power is taken at the 2.4 Hz resonance, for which we can use the bandwidth $f_{min} = 2.2\,\text{Hz}$ and $f_{max} = 2.6\,\text{Hz}$. While these may not specify an accurate frequency range for the event they can be used to calculate the proposed SNR1 and SNR2 metrics for the event catalogue. To this end, the Algorithm 2 was applied to the entire catalogue with these frequency bands and the parameters above.

Fig. 13 shows the comparison of the obtained SNR2 for the pressure and wind for each class of event (split into LF/BB and 2.4 Hz/HF/VF) to the PSD ratio calculated by the MQS team.

For the low frequency group of events (LF and BB) there is a strong relationship with power law exponents just under 1, against both atmospheric variables. This shows that the low amplitude events are actually generally very independent in this bandwidth and, while still significant, the SNR2 for the larger events is slightly lower owing to the averaging over the event of our method compared to the PSD based SNR. At lower SNRs the matched-moment values give a higher value, with the divergence from environmental injection more apparent than in the seismic signal alone, thus providing a higher degree of confidence.

In comparison, the higher frequency group shows a different relationship. The power law exponent is around 2 for the 2.4 Hz, VF and HF groups against both atmospheric variables. showing that the larger events tend to have a higher SNR2 than derived from the PSD and the lower SNR events have a lower SNR2 and are more difficult than low frequency events to distinguish from the environment. This suggests that this bandwidth is more susceptible to environmental injection and so smaller events are harder to distinguish from the background. This is in line with Section 4.3 which showed an increased environmental sensitivity with frequency.

The SNR derived from the pressure is often more robust than from wind. For example, in Fig. 13 the pressure based plots show a tighter clustering than the wind based. This is due to the the limitations of TWINS inherent to wind sensing. At wind speeds below the threshold of $2.8\,\text{m\,s}^{-1}$ the TWINS measurement can be inaccurate (Banfield et al., 2020). Moreover, the higher sample rate of the pressure sensor data is useful. As discussed in Section 4.3.3 we use the pressure envelope here as at least as a partial proxy for the dynamic pressure.

High frequency events have larger horizontal than vertical components, owing to their scattering nature (Lognonné et al., 2020). However, the 2.4 Hz resonance is vertically polarised and so we do not see this directly in the SNRs obtained with the fixed parameters for the catalogue. This feature can be seen though in the bandwidth specific analysis in the case of S0128a where we have chosen to display the SNR from the North component.

This implementation of the proposed SNR2 metric provides an automated system to assess events in the catalogue (InSight Marsquake Service, 2020) in terms of independence from environmental injection. As this is an automatic operational approach, some SNRs may not be truly accurate owing to the unpreventable data quality issues outlined above. Moreover, the implementation requires a set of fixed parameters as inputs for Algorithm 2. These parameters are outlined in Section 5.2.1 with the bandwidth $f_{min} = 0.2\,\text{Hz}$ to $f_{max} = 0.5\,\text{Hz}$ for the lower frequency group and $f_{min} = 2.2\,\text{Hz}$ to $f_{max} = 2.6\,\text{Hz}$ for the higher frequency events. However, on the whole this implementation has shown to be reasonably robust. This implementation therefore acts to provide a necessary reference for catalogue users to identify suitable events for their analysis and to understand their distribution in terms of environmental independence. Furthermore, a methodology is in

place where this analysis can be fine-tuned for a specific event. This is intimated in the sequel, Section 5.3. The SNRs for the entire catalogue are reported in Appendix A.
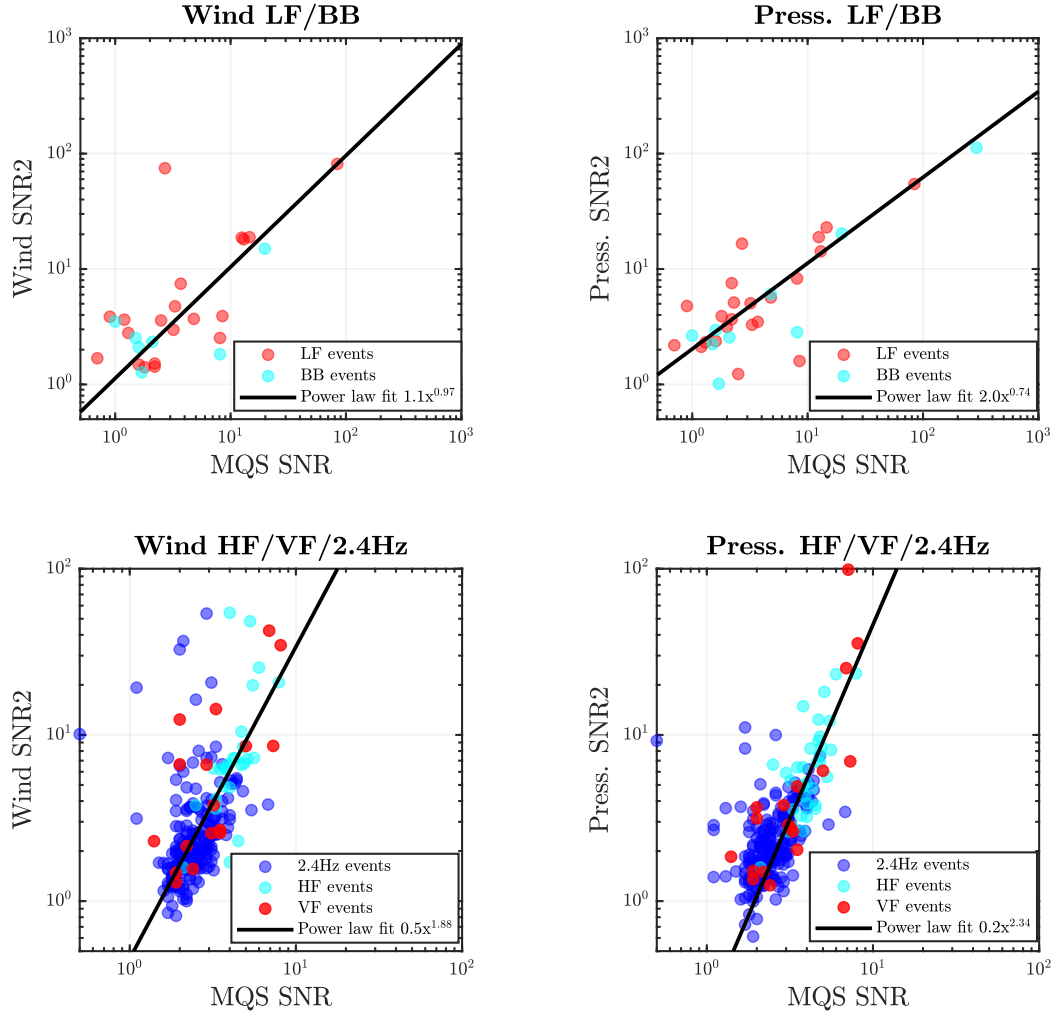
Figure 13: Comparison of SNR derivations from the proposed SNR2 metric and MQS calculated SNR. A power-law fit is plotted for both pressure and wind derived SNRs for each low and high frequency grouping.

5.3 Discrimination between atmospheric and other non-seismic source injections

We have proposed a method for event analysis based on a moving moment matching regression. This has been shown for event analysis and implemented as an automatic algorithm to obtain an SNR. In this section we employ this method more generally to identify episodes of loss in correlation in the energy transferred by wind or pressure to that of the observed seismic signal. This essentially transforms our empirical distributions, in this case the pressure and wind, to what we assume to be the theoretical one, or the reference one,

in this case the ground acceleration. It thus allows us to understand sources of empirical anomalies in the regression of these variables. Fig. 14 illustrates the seismic envelope against the matched pressure energy and wind speed over four distinct sols for various prominent features observed so far at the InSight landing site. Here we demonstrate how identification of a divergence in the moment-matched atmospheric and seismic envelopes (calculated here as the magnitude of the three-dimensional ZNE vector of the acceleration response as $\sqrt{(Z^2 + N^2 + E^2)}$ allows us to discriminate different potential sources of noise contamination to the combined seismic signal from all directions. Fig. 14a illustrates this approach for the Quality A, VF event on sol 128. The arrival of this particular VF event is seen with the seismic envelope diverging from the expected match, indicating that the signal source was not due to environmental injection. The seismic envelope during the event is significantly above the acceleration-equivalent environmental injection, suggesting a non-site source for the seismic signal, uncontaminated by wind or pressure energy. The robotic arm excursion can be seen following the event promptly, performing a manoeuvre from which the Instrument Deployment Camera (IDC) achieves the tau pose, in order to perform imaging for variations above the horizon in the atmospheric optical depth (Trebi-Ollennu et al., 2018).

An LF event from sol 133 can be seen diverging in Fig. 14b shortly after a broadband glitch, with both of these features indicating non-atmosphere origins. After the occurrence of some further VBB glitches later on, a 'pressure burst' diverges from the seismic and wind match. Pressure bursts are a rare phenomenon of nighttime occurrences exclusively observed on the pressure measurements with a source mechanism that is not yet understood (Banfield et al., 2020).

Fig. 14c demonstrates the discrimination between features of analogous spectral signatures from sol 253. A broadband impulse resulting from the robotic arm motion performing a push with the scoop onto the regolith is observed at 19:50 UTC. The signature resembles the 'glitch-like' spectral character of a weak convective vortex occurring at 20:10. Convective vortices are weather phenomena which induce a characteristic transient drop in the atmospheric pressure of various magnitudes and observed by SEIS as a tilt in the ground response (Kenda et al., 2017a; Murdoch et al., 2020). Notice how the broadband injection from the lander vibration induced by the robot arm motion is not observed in the atmospheric energy, in contrast to the vortex that is matched by the envelope forecasting equation. Another feature resemblance occurred from a different robotic arm motion during which the arm retracted further away from the surface at 20:01. The duration and high-frequency spectral characteristics are not dissimilar to the pressure energy injection three minutes later, marked as ΔPressure.

Donks, prominent impulse-like high-frequency features exciting lander resonances and described earlier as occurring intermittently at all time regimes of the day are seen on Fig. 14d for sol 334 during the sunset, apparent at frequencies above 8 Hz from the SP ZNE acceleration response magnitude. Amidst this forest of donks, a VF event S0334a occurs, which is divergent from the atmospheric match.
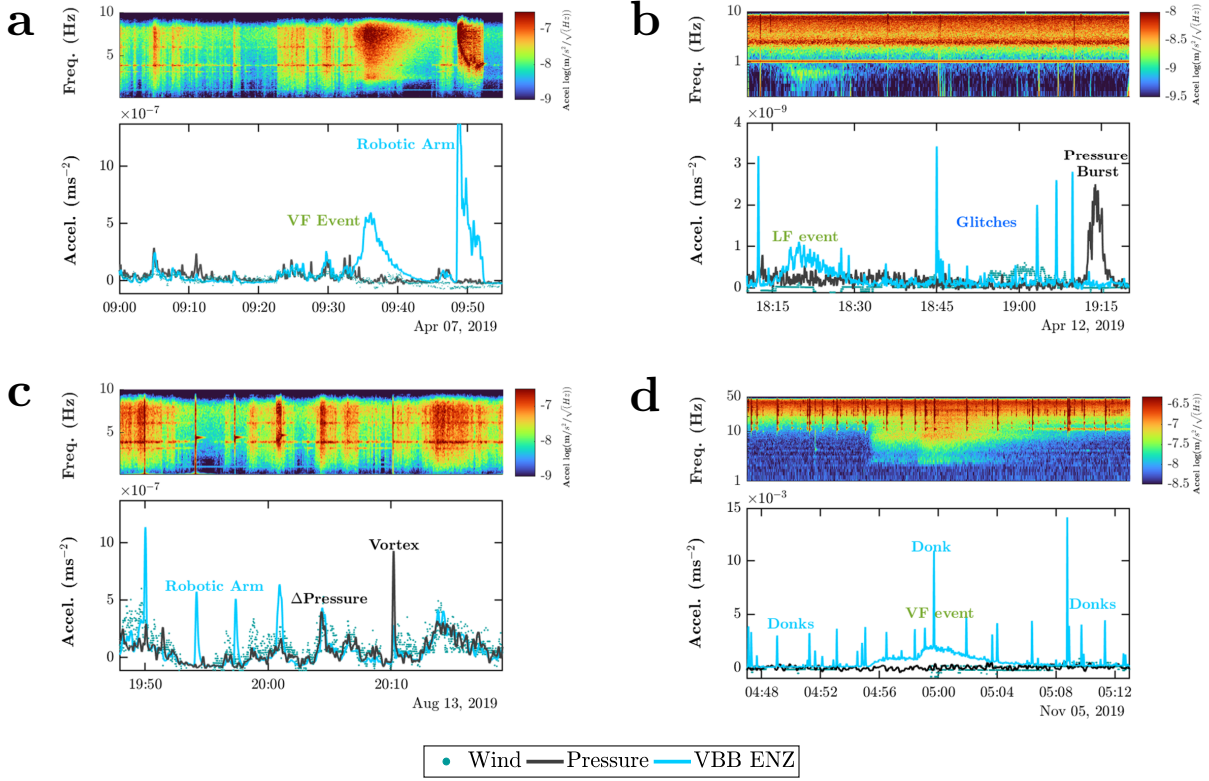
Figure 14: Discriminating origins of atmospheric injection from other sources at the InSight landing site. (a) Sol 128 - VF event and robotic arm motion switching to tau position. Frequency band applied 1 - 8 Hz (b) Sol 133 - Glitches, LF event and a 'pressure burst', a poorly understood excess energy injection for which SEIS is known to be insensitive to (Banfield et al., 2020). Frequency band applied 0.1 - 1 Hz. (c) Sol 154 - Robotic arm motion during which the scoop pushed onto the regolith. A pressure bump is seen later matching to the SEIS envelope, however, notice the similarity in the spectral character of the robotic arm motion 5 minutes before. A convective vortex at 20:10 appears 'glitch-like' - notice the resemblance of the vortex's signature to the HF spectral character of the regolith push at 19:50. Frequency band applied 1 - 8 Hz. (d) Sol 334 - a VF event amidst a forest of dinks and donks. Frequency band applied 5 - 40 Hz for the SP ENZ magnitude.

6 Discussion and Conclusion

The auxiliary sensors of InSight were part of the mission's design to help identify the effect of the atmosphere on the prime seismic payload of SEIS (W. Banerdt et al., 2013). However, the mapping between each sensor's data is not entirely straightforward for two major underlying physical reasons. Firstly, the coupling between the atmosphere and the lander is a result of the sum of the atmospheric forcing on all the surfaces of the lander and the regolith which will vary according to the wind direction and the level of turbulence (Murdoch et al., 2017; Teanby et al., 2017; Myhill et al., 2018). InSight's wind sensor's can only provide at most a two-point (at different locations and height than SEIS) measurement. Secondly, the transmission of the forces through the regolith to SEIS will depend on the multi-layer regolith (Golombek et al., 2020) properties that will in turn depend on the environment in the near-surface region. The quantification of the injection can therefore be seen as a hidden-variable problem, breaking the 1-1 mapping that might be hoped for between the environmental and seismic signals.

Two possible approaches to reveal these variables are through modelling and analogue testing. The first is challenging due to the geometrical and time resolution requirements to allow a convergence on the dynamics. Analogue testing would also be a major undertaking, requiring a representative model of the lander, regolith and atmosphere under Mars conditions. Furthermore, we are looking at environmental injection levels on Mars which are below the lowest observed background on Earth over much of our observational bandwidth: the deployment of SEIS was successful in physically attenuating environmental injection to levels better than can be observed in the quietest vault on Earth. Hence it is impossible to provide analogue testing that would elucidate injections at the levels we have observed with InSight, and assumptions of linearity would be required to to extrapolate from Earth testing to the mission environment.

The approach outlined in this work is instead to use the data itself to reveal the effect of these hidden variables as a time-dependent coupling between the environmental and seismic signals. We use the observed comodulation of the environmental and seismic signals to estimate the power transferred from the environment to SEIS. The method of moments applied here allows this coupling to be quantified within related regions even in the absence of an injective function which would provide a phase relationship between the signals to allow the estimation of a transfer function.

In terms of the qualitative relationship revealed, the environmental injection is generally broad band, except at the resonances of the lander, with the environmental signal variance at a broad range of frequencies injecting across much of the bandwidth of the seismic signals. Only during the quietest periods is the sensitivity of seismic detection set by the noise floor of the VBB and SP sensors of SEIS. The relationship between the signals varies with both the diurnal and seasonal cycle, with varying power laws identifiable as a function of frequency. The diurnal covariance is cyclic, with three seasonally evolving identifiable regimes of which the quiet evening period is of prime interest for seismic event detection on the planet.

This work has quantified the relationship by matching the first and second moments of the environmental and seismic signal variance in a time-advanced window longer than the observed duration of possible seismic events. Such a matching allows an estimated attribution of signal in these events between environmental and tectonic sources and the derivation of a corresponding environmental SNR. These SNRs shows that while the lower frequency events generally have a high enough SNR consistent with a tectonic source, at higher frequencies above 1 Hz many events show significant environmental injection.

The limitations of this approach are two-fold. Firstly, during the quietest periods the environmental sensors themselves are at the threshold for reliable quantification. It is therefore quite possible that environmental injection could still be occurring, but can only be detected on SEIS signals themselves. An extension of the existing approach would therefore be to use the broadband characteristics of the injection, and its enhancement at the known resonances of the lander to give an internal attribution; an excess energy at such a resonance comodulating with an environmentally undetectable signal would then allow an estimate of the partition of the signal energy between tectonic and environmental sources. The ability of the seismic signal to predict the wind speed and direction suggests the viability of such an approach.

While the physical attenuation of any environmental injection into a seismic signal is preferable, mission constraints will always limit the ability to provide such attenuation comparable to a terrestrial deployment. However, we show here that environmental sensors can provide a quantification of environmental injection, even if the pathway for such an injection is only partially understood. Sensors will usually levy a lighter resource burden on a mission than deployment mechanisms and in addition provide science return in their own right. Hence this work provides a motivation for including sufficient environmental sensors in future mission payloads to provide critical attenuation. The sensors should be chosen to measure the largest expected environmental injections, and have sufficient performance to

quantify the injection down to the seismic sensors' noise floor. However, even without such dedicated sensors, we have shown it is possible to use different bandwidths of seismic sensors for seismic and environmental attribution, providing an internal approach to quantify such injection, and thus effectively allowing SEIS itself to build its own virtual vault.

Acknowledgments

References

Anderson, D. L., Miller, W., Latham, G., Nakamura, Y., Toksöz, M., Dainty, A., ... Knight, T. (1977). Seismology on mars. *Journal of Geophysical Research*, *82*(28), 4524–4546.

Banerdt, W., Smrekar, S., Lognonné, P., Spohn, T., Asmar, S., Banfield, D., ... others (2013). Insight: a discovery mission to explore the interior of mars. In *Lunar and planetary science conference* (Vol. 44, p. 1915).

Banerdt, W. B., Smrekar, S. E., Banfield, D., Giardini, D., Golombek, M., Johnson, C. L., ... others (2020). Initial results from the insight mission on mars. *Nature Geoscience*, 1–7.

Banfield, D., Rodriguez-Manfredi, J. A., Russell, C. T., Rowe, K. M., Leneman, D., Lai, H. R., ... Banerdt, W. B. (2018, Dec 17). Insight auxiliary payload sensor suite (apss). *Space Science Reviews*, *215*(1), 4. Retrieved from `https://doi.org/10.1007/s11214-018-0570-x` doi: 10.1007/s11214-018-0570-x

Banfield, D., Spiga, A., Newman, C., Forget, F., Lemmon, M., Lorenz, R., ... others (2020). The atmosphere of mars as observed by insight. *Nature Geoscience*, 1–9.

Bollerslev, T. (1986). Generalized autoregressive conditional heteroskedasticity. *Journal of econometrics*, *31*(3), 307–327.

Bollerslev, T., Chou, R. Y., & Kroner, K. F. (1992). Arch modeling in finance: A review of the theory and empirical evidence. *Journal of econometrics*, *52*(1-2), 5–59.

Bruns, A., & Eckhorn, R. (2004). Task-related coupling from high-to low-frequency signals among visual cortical areas in human subdural recordings. *International journal of psychophysiology*, *51*(2), 97–116.

Buus, S. (1985). Release from masking caused by envelope fluctuations. *The Journal of the Acoustical Society of America*, *78*(6), 1958–1965.

Charalambous, C. (n.d.). On the evolution of particle fragmentation with applications to planetary surfaces.

Charalambous, C., McClean, J., Baker, M. M., Pike, T., Golombek, M. P., Lemmon, M. T., ... et al. (2020). Aeolian changes at the insight landing site on mars: Multi-instrument observations. *Earth and Space Science Open Archive*, 17. Retrieved from `https://doi.org/10.1002/essoar.10503003.1` doi: 10.1002/essoar.10503003.1

Davy, R., Davis, J. A., Taylor, P. A., Lange, C. F., Weng, W., Whiteway, J., & Gunnlaugson, H. P. (2010). Initial analysis of air temperature and related data from the Phoenix

MET station and their use in estimating turbulent heat fluxes. *Journal of Geophysical Research (Planets)*, *115*(E14), 0-+. doi: 10.1029/2009JE003444

De Angelis, S., & Bodin, P. (2012). Watching the wind: Seismic data contamination at long periods due to atmospheric pressure-field-induced tilting. *Bulletin of the Seismological Society of America*, *102*(3), 1255–1265.

DeGroot, M. H., & Schervish, M. J. (2012). *Probability and statistics.* Pearson Education.

Dybing, S. N., Ringler, A. T., Wilson, D. C., & Anthony, R. E. (2019). Characteristics and spatial variability of wind noise on near-surface broadband seismometers. *Bulletin of the Seismological Society of America*, *109*(3), 1082–1098.

Engle, R. F., & Sokalska, M. E. (2012). Forecasting intraday volatility in the us equity market. multiplicative component garch. *Journal of Financial Econometrics*, *10*(1), 54–83.

Garcia, R. F., Kenda, B., Kawamura, T., Spiga, A., Murdoch, N., Lognonné, P. H., . . . Banerdt, W. B. (2020). Pressure effects on SEIS-InSight instrument , improvement of seismic records and characterization of long period atmospheric waves from ground displacements. *Journal of Geophysical Research: Planets*.

Giardini, D., Lognonné, P., Banerdt, W. B., Pike, W. T., Christensen, U., Ceylan, S., . . . others (2020). The seismicity of mars. *Nature Geoscience*, *13*(3), 205–212.

Golombek, M., co authors, & the InSight team. (2020). Geology of the InSight landing site, Mars. *Nature Communications (in press)*. doi: 10.1038/s41467-020-14679-1

Hall, A. R. (2005). *Generalized method of moments.* Oxford university press.

Hall, J. W., Haggard, M. P., & Fernandes, M. A. (1984). Detection in noise by spectro-temporal pattern analysis. *The Journal of the Acoustical Society of America*, *76*(1), 50–56.

Hansen, L. P. (1982). Large sample properties of generalized method of moments estimators. *Econometrica: Journal of the Econometric Society*, 1029–1054.

Hess, S. L., Henry, R. M., Leovy, C. B., Ryan, J. A., & Tillman, J. E. (1977). Meteorological results from the surface of Mars: Viking 1 and 2. *J. Geophys. Res.*, *82*, 4559-4574.

Hutt, C. R., Ringler, A. T., & Gee, L. S. (2017). Broadband seismic noise attenuation versus depth at the albuquerque seismological laboratory. *Bulletin of the Seismological Society of America*, *107*(3), 1402–1412.

InSight Mars SEIS Data Service. (2019). *Seis raw data: Insight mission.* IPGP, JPL, CNES, ETHZ, ICL, MPS, ISAE-Supaero, LPG, MSFC. Retrieved from `https://doi.org/10.18715/SEIS.INSIGHT.XB_2016` doi: 10.18715/SEIS.INSIGHT.XB_2016

InSight Marsquake Service. (2020). *Mars seismic catalogue, insight mission; v2 2020-04-01.* ETHZ, IPGP, JPL, ICL, ISAE-Supaero, MPS, Univ. Bristol. Retrieved from `http://www.insight.ethz.ch/seismicity/catalog/v2` doi: 10.12686/a7

Johnson, C. W., Meng, H., Vernon, F., & Ben-Zion, Y. (2019). Characteristics of ground motion generated by wind interaction with trees, structures, and other surface obstacles. *Journal of Geophysical Research: Solid Earth*, *124*(8), 8519–8539.

Johnson, C. W., Vernon, F., Nakata, N., & Ben-Zion, Y. (2019). Atmospheric processes modulating noise in fairfield nodal 5 hz geophones. *Seismological Research Letters*, *90*(4), 1612–1618.

Kenda, B., Drilleau, M., Garcia, R., Kawamura, T., Murdoch, N., Compaire, N., . . . Widmer-Schnidrig, R. (2020). Subsurface structure at the insight landing site from compliance measurements by seismic and meteorological experiments. *Journal of Geophysical Research: Planets*, *submitted*.

Kenda, B., Lognonné, P., Spiga, A., Kawamura, T., Kedar, S., Banerdt, W. B., . . . Golombek, M. (2017a). Modeling of ground deformation and shallow surface waves generated by martian dust devils and perspectives for near-surface structure inversion. *Space Science Reviews*, *211*(1-4), 501–524.

Kenda, B., Lognonné, P., Spiga, A., Kawamura, T., Kedar, S., Banerdt, W. B., . . . Golombek, M. (2017b, Jun). Modeling of ground deformation and shallow surface waves generated by martian dust devils and perspectives for near-surface structure inversion. *Space Science Reviews*. doi: 10.1007/s11214-017-0378-0

Lognonné, P., Banerdt, W., Pike, W., Giardini, D., Christensen, U., Garcia, R., ... others (2020). Constraints on the shallow elastic and anelastic structure of mars from insight seismic data. *Nature Geoscience*, *13*(3), 213–220.

Lognonné, P., Banerdt, W. B., Giardini, D., Pike, W. T., Christensen, U., Laudet, P., ... Wookey, J. (2019, Jan 28). Seis: Insight's seismic experiment for internal structure of mars. *Space Science Reviews*, *215*(1), 12. Retrieved from `https://doi.org/10.1007/s11214-018-0574-6` doi: 10.1007/s11214-018-0574-6

Lognonné, P., & Mosser, B. (1993). Planetary seismology. *Surveys in Geophysics*, *14*, 239-302. doi: 10.1007/BF00690946

Lorenz, R. D., Nakamura, Y., & Murphy, J. R. (2017). Viking-2 seismometer measurements on mars: Pds data archive and meteorological applications. *Earth and Space Science*, *4*(11), 681–688.

Lott, F. F., Ritter, J. R., Al-Qaryouti, M., & Corsmeier, U. (2017). On the analysis of wind-induced noise in seismological recordings. *Pure and Applied Geophysics*, *174*(3), 1453–1470.

McGraw, R. (1997). Description of aerosol dynamics by the quadrature method of moments. *Aerosol Science and Technology*, *27*(2), 255–265.

Mimoun, D., Murdoch, N., Lognonné, P., Hurst, K., Pike, W. T., Hurley, J., ... others (2017). The noise model of the seis seismometer of the insight mission to mars. *Space Science Reviews*, *211*(1-4), 383–428.

Mueller, N., Knollenberg, J., & co authors. (2020). Calibration of the HP^3 radiometer on insight. *Earth and Space Science*. doi: 10.1029/2020EA001086

Murdoch, N., Alazard, D., Knapmeyer-Endrun, B., Teanby, N., & Myhill, R. (2018). Flexible mode modelling of the insight lander and consequences for the seis instrument. *Space Science Reviews*, *214*(8), 117.

Murdoch, N., Mimoun, D., Garcia, R. F., Rapin, W., Kawamura, T., Lognonné, P., ... Banerdt, W. B. (2017). Evaluating the wind-induced mechanical noise on the insight seismometers. *Space Science Reviews*, *211*(1-4), 429–455.

Murdoch, N., Spiga, L. R., A, Garcia, ., R, & Banerdt, W. B. (2020). Constraining martian regolith parameters and vortex trajectories from combined seismic and meteorological measurements. *Journal of Geophysical Research: Planets*, *submitted*.

Myhill, R., Teanby, N., Wookey, J., & Murdoch, N. (2018). Near-field seismic propagation and coupling through mars' regolith: implications for the insight mission. *Space Science Reviews*, *214*(5), 85.

Naderyan, V., Hickey, C. J., & Raspet, R. (2016). Wind-induced ground motion. *Journal of Geophysical Research: Solid Earth*, *121*(2), 917–930.

Panning, M. P., Pike, W. T., Lognonné, P., Banerdt, W. B., Murdoch, N., Banfield, D., ... others (2020). On-deck seismology: Lessons from insight for future planetary seismology. *Journal of Geophysical Research: Planets*, e2019JE006353.

Pearson, K. (1894). Contributions to the mathematical theory of evolution. *Philosophical Transactions of the Royal Society of London. A*, *185*, 71–110.

Richards, V. M. (1987). Monaural envelope correlation perception. *The Journal of the Acoustical Society of America*, *82*(5), 1621–1630.

Ringler, A. T., Steim, J., Wilson, D. C., Widmer-Schnidrig, R., & Anthony, R. E. (2020). Improvements in seismic resolution and current limitations in the global seismographic network. *Geophysical Journal International*, *220*(1), 508–521.

Schofield, J. T., Crisp, D., Barnes, J. R., Haberle, R. M., Magalhaães, J. A., Murphy, J. R., ... Wilson, G. (1997). The Mars Pathfinder Atmospheric Structure Investigation/Meteorology (ASI/MET) experiment. *Science*, *278*, 1752-1757.

Scholz, J.-R., Widmer-Schnidrig, R., Davis, P., Lognonne, P., Pinot, B., Garcia, R. F., ... Banerdt, W. B. (2020). Detection, analysis and removal of glitches from InSight's seismic data from Mars. *Journal of Geophysical Research: Planets*, *submitted*.

Shirvalkar, P. R., Rapp, P. R., & Shapiro, M. L. (2010). Bidirectional changes to hippocampal theta–gamma comodulation predict memory for recent spatial episodes. *Proceedings of the National Academy of Sciences*, *107*(15), 7054–7059.

Sorrells, G., McDonald, J. A., Der, Z., & Herrin, E. (1971). Earth motion caused by local atmospheric pressure changes. *Geophysical Journal International*, *26*(1-4), 83–98.

Sorrells, G. G. (1971). A preliminary investigation into the relationship between long-period seismic noise and local fluctuations in the atmospheric pressure field. *Geophysical Journal International*, *26*(1-4), 71–82.

Sorrells, G. G., & Goforth, T. (1973). Low-frequency earth motion generated by slowly propagating partially organized pressure fields. *Bulletin of the Seismological Society of America*, *63*(5), 1583–1601.

Spiga, A., Banfield, D., Teanby, N. A., Forget, F., Lucas, A., Kenda, B., . . . Banerdt, W. B. (2018). Atmospheric Science with InSight. *Space Science Reviews*, *214*, 109. doi: 10.1007/s11214-018-0543-0

Spiga, A., Murdoch, N., Lorenz, R., Forget, F., Newman, C., Rodriguez, S., . . . Banerdt, W. B. (2020, May). A study of daytime convective vortices and turbulence in the martian Planetary Boundary Layer based on half-a-year of InSight atmospheric measurements and Large-Eddy Simulations. *arXiv e-prints*, arXiv:2005.01134.

Stähler, S. C., Schmidt-Aursch, M. C., Hein, G., & Mars, R. (2018). A self-noise model for the german depas obs pool. *Seismological Research Letters*, *89*(5), 1838–1845.

Sutton, J. L., Leovy, C. B., & Tillman, J. E. (1978). Diurnal variations of the Martian surface layer meteorological parameters during the first 45 sols at two Viking lander sites. *J. Atmos. Sci.*, *35*, 2346-2355.

Teanby, N., Stevanović, J., Wookey, J., Murdoch, N., Hurley, J., Myhill, R., . . . Pike, W. T. (2017). Seismic coupling of short-period wind noise through mars' regolith for nasa's insight lander. *Space Science Reviews*, *211*(1-4), 485–500.

Trebi-Ollennu, A., Kim, W., Ali, K., Khan, O., Sorice, C., Bailey, P., . . . others (2018). Insight mars lander robotics instrument deployment system. *Space Science Reviews*, *214*(5), 93.

Verhey, J. L., Pressnitzer, D., & Winter, I. M. (2003). The psychophysics and physiology of comodulation masking release. *Experimental Brain Research*, *153*(4), 405–417.

Withers, M. M., Aster, R. C., Young, C. J., & Chael, E. P. (1996). High-frequency analysis of seismic background noise as a function of wind speed and shallow depth. *Bulletin of the Seismological Society of America*, *86*(5), 1507–1515.

Wolin, E., van der Lee, S., Bollmann, T. A., Wiens, D. A., Revenaugh, J., Darbyshire, F. A., . . . Wysession, M. E. (2015). Seasonal and diurnal variations in long-period noise at spree stations: The influence of soil characteristics on shallow stations' performance. *Bulletin of the Seismological Society of America*, *105*(5), 2433–2452.

Ziolkowski, A. (1973). Prediction and suppression of long-period nonpropagating seismic noise. *Bulletin of the Seismological Society of America*, *63*(3), 937–958.

Zürn, W., & Widmer, R. (1995). On noise reduction in vertical seismic records below 2 mhz using local barometric pressure. *Geophysical Research Letters*, *22*(24), 3537–3540.

Appendix A Marsquake catalogue SNRs

1286

Event Name	MQS SNR	Mean Wind	SNR2 Wind	SNR2 Press.
S0377c	2.50	2.87	3.59	1.23
S0357a	1.80	1.10	1.41	3.91
S0345a	2.20	1.48	1.51	3.67
S0330a	12.50	2.71	18.71	18.90
S0329b	2.30	2.12	0.06	5.12
S0327d	2.20	3.43	1.43	7.55
S0325a	14.60	3.63	18.87	22.93
S0323d	2.70	1.97	74.72	16.59
S0320b	3.70	1.78	7.46	3.48
S0290b	0.90	2.19	3.86	4.78
S0254b	1.20	2.05	3.64	2.12
S0251a	13.00	0.96	18.09	14.22
S0240a	1.70	-	-	-
S0234c	0.70	1.87	1.69	2.19
S0226b	3.30	1.20	4.75	3.28
S0205a	2.00	1.93	-	3.15
S0201a	1.60	0.90	1.49	2.37
S0189a	1.30	2.48	2.79	2.31
S0185a	4.80	2.31	3.70	5.67
S0183a	3.20	2.24	2.97	5.05
S0173a	84.10	3.30	81.40	54.50
S0171a	1.30	-	-	-
S0167b	4.20	3.72	-	-
S0167a	8.50	2.58	3.91	1.60
S0105a	8.10	2.48	2.53	8.28

Table A1: LF SNR Table. (MQS Catalogue V2, doi:10.12686/a7)

Event Name	MQS SNR	Mean Wind	SNR2 Wind	SNR2 Press.
S0362b	1.00	1.42	3.51	2.65
S0235c	1.70	0.42	1.27	1.01
S0235b	290.50	0.78	-	112.46
S0234d	1.60	2.78	2.10	2.96
S0217a	1.50	1.36	2.53	2.23
S0154a	19.80	2.46	15.01	20.28
S0152a	2.10	2.76	2.34	2.55
S0133a	4.80	1.75	-	6.06
S0132a	8.10	3.76	1.83	2.83

Table A2: BB SNR Table.(MQS Catalogue V2, doi:10.12686/a7)

Event Name	MQS SNR	Mean Wind	SNR2 Wind	SNR2 Press.
S0385a	3.00	0.44	-	5.91
S0384d	2.50	-	-	-
S0384c	3.20	-	-	-
S0384b	5.30	-	-	-
S0375a	4.70	2.41	10.48	9.24
S0371b	3.90	2.29	6.65	4.30
S0363d	3.10	1.60	329.99	2.62
S0361c	4.60	2.21	-	6.88
S0360b	2.10	1.38	1.59	1.59
S0352a	4.80	2.18	8.47	7.54
S0351b	4.00	1.45	54.32	5.17
S0349a	4.00	1.94	4.82	3.88
S0347a	5.50	2.08	19.90	12.13
S0343b	4.50	1.48	-	3.59
S0340a	3.20	1.35	6.28	5.30
S0331a	6.00	3.04	25.40	23.19
S0327c	5.30	2.16	48.27	5.58
S0325b	4.90	2.61	6.75	8.50
S0324a	2.50	3.61	3.78	6.62
S0323a	3.80	2.05	6.38	2.64
S0319b	4.30	2.06	7.24	4.78
S0319a	3.30	2.33	4.14	2.78
S0315b	4.00	1.21	1.71	3.21
S0314b	4.80	1.55	-	9.78
S0311a	5.10	1.62	7.16	18.15
S0308a	4.70	3.21	6.58	12.37
S0306a	3.70	3.08	4.91	3.27
S0304b	5.60	2.25	7.27	8.13
S0303a	3.50	1.88	6.19	6.38
S0292a	-	-	-	-
S0291c	4.20	2.18	7.24	8.29
S0289a	7.90	2.80	20.74	23.44
S0262b	3.80	2.53	6.27	6.40
S0260a	-	-	-	-
S0246a	4.60	-	-	-
S0239a	4.80	0.34	1.67	6.78
S0231b	4.30	-	-	-
S0228c	4.50	2.54	2.30	3.79
S0213a	3.80	2.13	381.14	14.89
S0202c	3.30	2.15	3.60	3.57
S0185b	3.80	2.58	6.18	4.88

Table A3: HF SNR Table. (MQS Catalogue V2, doi:10.12686/a7)

Event Name	MQS SNR	Mean Wind	SNR2 Wind	SNR2 Press.
S0387a	3.50	1.86	2.58	4.89
S0376a	3.50	3.32	2.68	2.04
S0367a	2.00	3.26	12.38	3.66
S0358c	3.20	2.23	3.78	2.76
S0346a	2.20	0.64	2.14	1.50
S0343a	2.90	1.27	6.62	3.77
S0334c	1.90	2.21	1.30	1.52
S0334b	2.40	2.34	1.56	1.24
S0334a	6.90	1.71	42.39	25.22
S0306c	1.40	1.77	2.30	1.85
S0301b	1.90	2.33	1.48	1.35
S0264e	8.10	3.04	34.65	35.59
S0263a	7.30	2.64	8.59	6.93
S0241a	2.00	0.48	6.65	3.14
S0226a	3.10	0.26	2.56	2.88
S0218a	5.00	3.09	8.57	6.09
S0202b	3.30	1.14	14.31	2.62
S0128a	7.10	4.53	304.91	98.76

Table A4: VF SNR Table. (MQS Catalogue V2, doi:10.12686/a7)

Event Name	MQS SNR	Mean Wind	SNR2 Wind	SNR2 Press.
S0389a	2.10	-	-	-
S0388b	1.70	2.89	1.06	1.05
S0388a	1.90	0.55	1.97	1.64
S0386b	2.50	3.00	2.07	1.86
S0386a	2.10	0.76	1.57	1.73
S0385c	3.20	-	-	-
S0385b	2.30	0.60	3.67	1.67
S0384a	2.70	-	-	-
S0383c	2.60	2.59	1.80	1.85
S0383b	1.80	2.46	1.40	1.26
S0383a	2.90	2.68	1.90	2.18
S0382a	1.80	2.87	1.35	2.84
S0381f	1.80	2.80	1.24	1.31
S0381e	2.00	2.41	6.51	1.72
S0381d	2.50	0.63	2.29	2.75
S0381c	2.00	2.47	2.36	1.84
S0381b	1.80	0.71	1.21	1.82
S0381a	2.30	0.50	1.88	2.88
S0380a	2.90	2.92	2.06	1.91
S0379b	2.10	2.24	2.28	1.52
S0379a	2.40	2.39	2.03	1.42
S0378b	3.60	2.48	3.46	4.32
S0378a	2.70	1.26	-	3.36
S0377b	1.80	2.64	1.60	1.36
S0377a	1.90	1.48	1.24	0.99
S0376b	2.60	3.03	1.58	1.32
S0374a	2.00	-	-	-
S0374b	1.70	-	-	-
S0373b	2.80	2.87	-	-
S0373a	2.00	-	-	-
S0372a	4.30	2.12	5.11	3.97
S0371a	1.90	0.76	2.82	1.70
S0370a	3.70	-	-	-
S0369c	1.70	-	-	-
S0369b	2.70	-	-	-
S0369a	1.70	-	-	-
S0368a	1.70	-	-	-
S0367d	2.10	1.96	-	1.68
S0367c	2.40	1.54	2.00	2.69
S0367b	2.10	1.51	1.23	1.36
S0366e	3.20	-	-	-
S0366d	2.20	-	-	-
S0366c	3.00	-	-	-
S0366b	2.10	-	-	-
S0366a	5.50	-	-	-
S0365b	2.60	2.24	1.65	1.02
S0365a	3.90	2.15	2.77	2.64
S0365c	2.20	1.04	2.85	1.90
S0364a	2.20	2.22	2.23	2.46
S0363c	2.70	0.54	3.43	1.68
S0363b	2.20	0.59	3.57	1.57
S0363a	3.30	2.31	2.76	4.25
S0362c	1.70	2.29	1.29	1.59
S0362a	2.10	0.50	1.61	1.44
S0361b	2.50	1.12	1.67	1.42
S0361a	2.50	3.76	16.31	-
S0360a	2.20	1.94	4.83	2.62
S0359a	2.50	1.77	1.60	1.34
S0358b	2.00	1.44	32.69	1.41
S0358a	2.00	2.06	1.69	1.74
S0357b	2.30	2.39	2.29	1.65
S0355a	2.90	2.63	53.7	3.16
S0354a	3.10	3.85	2.57	3.12
S0353d	2.50	3.43	1.96	1.38
S0353c	2.20	1.85	2.06	1.54
S0353b	2.60	1.75	8.02	4.49
S0353a	2.20	0.50	2.62	2.05
S0353f	1.10	3.06	447.20	2.68

Table A5: 2.4 Hz event SNR Table part 1 (MQS Catalogue V2, doi:10.12686/a7)

Event Name	MQS SNR	Mean Wind	SNR2 Wind	SNR2 Press.
S0353e	1.90	3.32	4.05	3.10
S0352b	2.20	1.85	-	1.75
S0350a	3.10	1.61	2.86	3.97
S0349b	2.40	4.13	2.53	2.43
S0348d	2.10	2.80	1.18	1.25
S0348c	3.20	1.93	3.11	2.33
S0348b	3.10	2.11	4.06	2.92
S0348a	2.50	1.14	1.35	2.14
S0346d	2.40	2.37	2.00	2.95
S0346c	2.10	2.18	1.80	1.67
S0346b	1.90	2.20	1.60	1.05
S0345b	2.50	2.95	2.20	1.85
S0345d	1.90	2.01	1.23	0.61
S0345c	1.90	1.46	5.37	1.24
S0344b	1.10	0.26	3.14	1.40
S0344a	2.40	0.32	6.82	1.81
S0342a	3.10	1.59	188.83	2.33
S0341a	2.10	1.75	-	2.12
S0340b	2.70	2.09	1.77	2.07
S0339f	1.30	1.24	298.47	3.63
S0339b	1.70	1.92	1.68	1.30
S0339a	1.80	1.95	1.24	1.71
S0339e	1.50	0.97	1.70	1.51
S0339d	1.70	1.86	1.55	1.47
S0339c	2.10	1.50	36.69	2.27
S0338b	4.10	1.35	5.08	5.08
S0338a	3.30	2.77	3.23	3.99
S0337a	2.90	2.32	3.73	3.30
S0335b	2.00	2.17	1.94	0.78
S0335c	1.80	1.81	1.26	1.36
S0335a	1.90	1.24	1.22	1.67
S0333a	2.20	2.50	1.75	1.62
S0332a	3.10	0.72	2.03	1.93
S0331b	3.80	2.19	2.50	3.97
S0329a	2.90	1.95	4.16	3.31
S0327b	2.60	1.99	1.83	1.76
S0327a	3.00	0.52	2.46	1.94
S0325d	4.40	2.71	5.48	5.30
S0325e	2.00	1.82	1.78	1.41
S0325c	2.60	2.13	1.30	2.18
S0324e	2.00	2.54	1.92	2.78
S0324d	2.40	0.79	1.89	1.57
S0324c	3.60	2.78	6.67	4.73
S0324b	1.90	3.63	1.44	1.34
S0323c	2.40	2.00	1.84	1.83
S0323b	2.80	2.09	2.04	2.65
S0322a	2.60	2.80	2.59	2.61
S0321a	2.20	-	-	-
S0320a	4.40	2.67	5.34	4.66
S0318a	3.10	2.14	2.81	2.70
S0315d	2.10	2.08	2.10	2.10
S0315c	1.90	0.98	1.92	1.88
S0315a	2.80	3.17	2.65	3.67
S0314a	3.20	0.96	3.18	2.31
S0313a	1.10	2.69	19.25	2.86
S0312b	2.00	1.94	1.84	1.60
S0312a	2.30	2.10	1.42	1.65
S0311b	3.60	2.04	3.98	2.34
S0310a	2.20	0.33	-	3.88
S0309c	2.20	2.28	2.53	1.43
S0309b	2.90	2.26	1.79	2.99
S0309a	3.10	1.94	7.34	3.37
S0308b	3.40	1.94	-	-
S0306d	1.90	3.30	3.48	3.49
S0305a	2.00	1.89	2.36	1.06
S0304a	3.90	1.48	4.17	4.29
S0304c	3.30	1.37	8.49	1.43
S0303b	2.10	0.81	-	1.65
S0302d	2.00	2.42	1.29	1.37
S0302c	2.10	2.08	1.59	1.31
S0302b	1.70	1.92	194.78	8.29
S0302a	2.10	2.02	1.82	2.11
S0301a	4.00	2.85	3.29	3.72
S0300a	3.00	2.07	2.43	1.86
S0299b	3.00	1.87	2.39	1.87

Table A6: 2.4 Hz event SNR Table part 2.(MQS Catalogue V2, doi:10.12686/a7)

Event Name	MQS SNR	Mean Wind	SNR2 Wind	SNR2 Press.
S0299a	2.90	-	-	-
S0298b	0.00	-	-	-
S0298a	8.50	-	-	-
S0297e	2.30	2.27	1.35	1.68
S0297d	1.90	2.20	-	1.37
S0297c	2.90	2.30	2.10	1.15
S0297b	2.70	-	-	-
S0297a	3.20	-	-	-
S0295b	2.90	2.33	1.58	1.30
S0295a	4.60	3.39	-	1.74
S0294b	1.70	2.86	7.26	11.09
S0294a	0.50	2.00	10.11	9.22
S0292c	2.60	-	-	-
S0292b	1.90	-	-	-
S0291d	2.30	2.22	2.02	2.20
S0291b	2.90	1.92	2.23	1.66
S0291a	2.20	3.99	2.10	3.80
S0290a	3.10	1.74	20.65	1.72
S0289b	2.50	2.56	1.99	1.76
S0266e	0.00	-	-	-
S0266d	0.00	-	-	-
S0266c	0.00	-	-	-
S0266b	2.00	-	-	-
S0265e	2.30	2.01	1.63	1.93
S0265d	2.50	1.90	2.57	1.84
S0265c	2.20	1.91	2.08	1.86
S0265b	3.70	1.98	-	2.47
S0265a	1.30	0.57	-	1.41
S0264d	2.50	1.88	3.68	2.09
S0264c	1.90	-	-	-
S0264b	3.20	-	-	-
S0264a	2.50	-	-	-
S0263c	2.90	2.08	3.32	2.27
S0263b	1.80	1.94	1.43	0.83
S0261b	4.80	1.96	4.58	7.48
S0261a	3.00	1.16	1.61	2.56
S0260b	2.80	-	-	-
S0257c	2.30	1.86	1.95	1.43
S0257b	4.10	1.93	-	6.20
S0257a	2.60	0.25	-	4.33
S0256c	2.50	2.29	2.41	2.91
S0256a	2.20	1.62	1.54	1.45
S0256b	3.00	3.44	2.18	2.98
S0255b	3.10	2.30	2.13	2.97
S0255a	1.90	1.84	1.63	2.13
S0254c	2.40	2.65	3.87	1.97
S0254a	2.90	1.60	7.27	2.19
S0253b	1.90	1.56	825.78	1.60
S0253a	1.90	1.59	2.12	2.18
S0252a	4.10	1.84	5.31	4.20
S0252b	1.60	0.25	1.15	3.69
S0251c	2.20	1.31	1.03	1.24
S0251b	1.80	0.32	1.36	2.60
S0250b	6.80	2.41	3.81	3.44
S0250a	2.30	0.77	1.54	2.29
S0249a	1.90	0.67	2.02	1.54
S0248d	2.00	2.69	2.05	1.40
S0248b	2.50	1.30	4.75	1.70
S0248a	2.80	1.78	2.43	1.39
S0248c	2.30	3.37	2.32	3.09
S0247b	2.00	2.67	1.19	1.64
S0247a	3.20	2.18	1.90	2.67
S0246b	2.20	-	-	-
S0244d	3.40	2.24	2.53	4.14
S0244e	2.10	1.72	-	1.52
S0244c	2.70	1.01	1.58	1.92
S0244b	2.40	0.58	2.13	2.54
S0244a	2.10	2.28	-	2.13
S0242d	1.70	1.99	0.85	0.72
S0242b	2.10	0.86	1.94	2.27
S0242a	4.00	1.67	3.10	3.62
S0242c	2.10	2.99	6.01	5.05
S0241b	2.10	2.36	2.02	1.55
S0240b	3.50	3.07	5.19	4.60
S0238a	1.90	1.32	0.82	1.36

Table A7: 2.4 Hz event SNR Table part 3. (MQS Catalogue V2, doi:10.12686/a7)

Event Name	MQS SNR	Mean Wind	SNR2 Wind	SNR2 Press.
S0237a	2.40	1.96	1.19	1.78
S0236b	1.90	1.84	1.64	1.16
S0236a	2.70	0.53	-	-
S0235d	2.50	2.09	1.99	1.96
S0235a	2.10	1.65	1.03	1.62
S0234b	2.00	1.60	1.14	1.19
S0234a	3.40	0.68	-	5.17
S0233a	1.80	1.49	0.94	1.90
S0231a	2.20	-	-	-
S0229a	2.80	0.71	2.46	1.77
S0228b	2.20	1.72	3.49	2.66
S0228a	2.10	0.33	1.60	1.60
S0227d	3.20	2.20	1.53	2.66
S0227c	2.10	1.06	2.09	1.47
S0227b	1.70	1.63	1.24	1.35
S0227a	1.60	0.51	1.70	1.02
S0226c	1.80	0.59	1.93	1.69
S0225a	2.00	1.49	1.46	1.70
S0222a	3.60	0.36	3.13	2.65
S0221c	1.80	1.65	314.86	1.09
S0221b	2.50	1.98	-	2.07
S0221a	2.90	3.24	2.99	3.26
S0219c	3.00	1.98	2.91	2.07
S0219b	3.20	1.19	-	2.97
S0219a	2.10	1.92	-	2.59
S0216c	1.80	-	-	-
S0216a	3.50	-	-	-
S0216b	3.10	3.13	1.73	3.26
S0215b	2.20	1.40	1.10	1.23
S0215a	2.40	1.38	2.10	2.05
S0212c	2.40	1.87	2.65	2.35
S0212b	2.60	1.84	3.61	9.99
S0212a	2.70	3.12	3.08	3.26
S0211a	2.70	2.04	2.12	1.98
S0211b	2.30	1.25	3.67	1.42
S0204a	5.40	2.65	3.53	2.89
S0203b	2.00	2.25	2.80	2.39
S0203a	1.70	1.27	1.57	1.86
S0202a	2.00	1.85	1.71	-
S0201b	2.30	1.77	1.60	1.68
S0200a	2.50	2.28	1.61	1.75
S0197a	2.10	1.98	1.64	1.28
S0194d	3.30	3.18	2.51	3.65
S0194c	3.10	2.04	2.46	4.85
S0194b	2.00	1.86	-	1.43
S0194a	2.20	1.60	1.00	2.30
S0193a	2.70	1.76	1.91	1.22
S0191a	2.70	2.68	2.01	1.92
S0186a	2.00	-	-	-
S0186b	3.60	-	-	-
S0183b	2.70	-	-	-
S0182a	2.00	-	-	-
S0168a	2.70	-	-	-
S0151a	2.50	-	-	-
S0116a	2.70	-	-	-

Table A8: 2.4 Hz event SNR Table part 4. (MQS Catalogue V2, doi:10.12686/a7)